

1

2

3

4

Cosmic ray validation of electrode positions in small-strip thin gap chambers for the upgrade of the ATLAS detector

5

Lia Formenti

6

7

8

Department of Physics
McGill University, Montreal
October, 2021

9

10

11

12

13

A thesis submitted to
McGill University
in partial fulfillment of the
requirements of the degree of
Master of Science

¹⁵ Table of Contents

¹⁶ 1	Introduction	1
¹⁷ 2	High energy particle physics at the LHC and the ATLAS experiment	4
¹⁸ 2.1	The Standard Model	4
¹⁹ 2.2	Beyond the Standard Model	6
²⁰ 2.3	Studying high energy particle physics with accelerators	7
²¹ 2.4	The Large Hadron Collider	9
²² 2.5	Luminosity	9
²³ 2.6	The High-luminosity LHC	10
²⁴ 2.7	The ATLAS experiment	10
²⁵ 3	The New Small Wheels	17
²⁶ 3.1	Motivation for the New Small Wheels (NSWs)	17
²⁷ 3.2	Design of the NSWs	19
²⁸ 3.3	Small-strip thin gap chambers	21
²⁹ 3.4	sTGC Quadruplet Construction	22
³⁰ 3.5	NSW alignment	25
³¹ 4	Using cosmic muons to measure relative strip position offsets	28
³² 4.1	Cosmic rays	28
³³ 4.2	Experimental setup	29

34	4.3 Data acquisition	30
35	4.4 Data preparation	30
36	4.4.1 Cuts on electrode hits	30
37	4.4.2 Clustering and tracking	31
38	4.5 Measuring relative local offsets	33
39	4.6 Visualizing relative alignment between layers	36
40	4.7 Systematic uncertainty	38
41	4.8 Discussion	40
42	5 Using x-rays to measure relative strip position offsets	41
43	5.1 Experimental setup	41
44	5.2 Data acquisition	43
45	5.3 Data preparation	43
46	5.4 Measuring local offsets	43
47	5.5 Measuring relative local offsets	45
48	6 Comparing cosmic muon and x-ray relative strip position offsets	49
49	6.1 Assessing correlation	49
50	6.2 Discussion	54
51	7 Outlook and summary	56
52	7.1 Outlook	56
53	7.2 Summary	57
54	References	58
55	APPENDICES	66
56	A Cluster position uncertainty	67
57	A.1 Cluster definition	67
58	A.2 Effect of fit algorithm on cluster mean	67
59	A.3 Effect of uncertainty in cluster mean on track residuals	68

60	B Analysis statistics	69
61	C Analysis systematics	71
62	C.1 Residual distribution fit function	71
63	C.2 Cosmic muon data collection voltage	72
64	C.3 Cluster fit algorithm	74
65	C.4 Differential non-linearity	75
66	D Printable plots	78

Abstract

68 The Large Hadron Collider (LHC) is used to generate subatomic physics processes at the
69 energy frontier to challenge our understanding of the Standard Model of particle physics.
70 The particle collision rate at the LHC will be increased up to seven times its design value in
71 2025-2027 by an extensive upgrade program. The innermost endcaps of the ATLAS muon
72 spectrometer consist of two wheels of muon detectors that must be replaced to maintain
73 the muon momentum resolution in the high-rate environment. The so-called New Small
74 Wheels (NSWs) are made of two detector technologies: micromegas and small-strip thin gap
75 chambers (sTGCs). The sTGCs are gas ionization chambers that hold a thin volume of gas
76 between two cathode boards. One board is segmented into copper readout strips of 3.2 mm
77 pitch that are used to precisely reconstruct the coordinate of a passing muon. Modules of
78 four sTGCs glued together into quadruplets cover the NSWs. Quadruplets were designed
79 to achieve a 1 mrad angular resolution to fulfill the spectrometer's triggering and precision
80 tracking requirements. To achieve the required angular resolution the absolute position of
81 the readout strips must be known in the ATLAS coordinate system to within 100 μm . At
82 McGill University, the performance of sTGC quadruplets was characterized using cosmic ray
83 data before being sent to CERN, where the charge profile left by x-rays is used to measure
84 the offset of the strip patterns with respect to nominal at a limited number of points on
85 the surface of each quadruplet. The x-ray strip position measurements have acceptable but
86 limited precision and do not span the whole area of the strip layers. Given the importance of
87 knowing the absolute position of each readout strip to achieve the performance requirements
88 of the NSWs, the x-ray method must be validated by an independent method. Cosmic ray
89 data is used to characterize the relative alignment between layers and validate the x-ray
90 method.

Résumé

Le collisioneur LHC est utilisé pour générer des processus de la physique subatomique à la frontière d'énergie pour remettre en cause le modèle standard de la physique des particules. Le taux des collisions du collisioneur LHC augmentera jusqu'à sept fois le taux nominal en 2025-2027 par un programme d'amélioration majeur et varié. Une partie du spectromètre à muons est composée de deux roues de détecteurs de muons qu'il faut remplacer pour maintenir la résolution d'élan après l'augmentation du taux. Appelées les Nouvelles Petites Roues (NSWs), elles en utilisent deux technologies: des chambres micromegas et des chambres sTGCs (chambres à petites bandes et à intervalles fins). Les sTGCs sont des chambres d'ionisation de gaz, qui contiennent un volume de gaz fin entre deux panneaux cathodiques. Un panneau est segmenté à petites bandes en cuivre avec une pente de 3.2 mm qui se servent comme des voies de signal pour reconstruire précisément la coordonnée d'un muon qui passe. Des modules de quatre sTGCs collés ensemble en quadruplets couvrent les NSWs. Les quadruplets étaient conçus pour réaliser une résolution angulaire de 1 mrad pour satisfaire les exigences des systèmes de déclenchement et de mesures de précision. Pour réaliser la résolution angulaire il faut que la position absolue de chaque bande soit connue dans ATLAS avec une précision à moins de 100 μm . À l'Université de McGill, la performance des quadruplets étaient caractériser avec des rayons cosmiques avant les envoyer à CERN, où le profil de charge laisser par des rayons-X est utilisé pour mesurer le déplacement du motif des bandes par rapport à nominal à un nombre de position limité sur la surface des quadruplets. Les déplacements mesurés pas les rayons-X ont une précision acceptable mais limitée, et ne couvrent pas la région entière des panneaux. Étant donné l'importance de savoir la position absolue de chaque bande pour réaliser les exigences de performance des NSWs, il faut une méthode indépendante pour valider la méthode des rayons-X. Les données recueillies avec les rayons cosmiques sont utilisées pour charactariser l'alignement relatif entre les panneaux et pour valider la méthode des rayons-X.

Acknowledgements

- 118 Experimental particle physics projects are never done alone. I am grateful to have been
119 working with the ATLAS Collaboration for two years now.
- 120 Thank you to Dr. Brigitte Vachon for her guidance throughout this project and for editing
121 this thesis. I am consistently amazed by her ability to jump into the details of my project
122 and discuss them with me.
- 123 Thanks also to Dr. Benoit Lefebvre, who collected some of the data used in this thesis, wrote
124 several software tools I used to analyze the data and advised me several times throughout
125 this project.
- 126 Thank you to my labmates at McGill University, Dr. Tony Kwan, Kathrin Brunner, John
127 McGowan and Charlie Chen. Kathrin taught me mechanical skills that I will apply elsewhere.
128 Tony, manager of the laboratory, created the most encouraging, trusting and productive work
129 environment I have ever been apart of.
- 130 Thank you to the friends I can call on at anytime, and thank you to my family whose
131 constant support makes every step possible.

Contribution of authors

I, the author, was involved in collecting the cosmic ray data from September 2019 - March 2021. I did not design the cosmic ray testing procedure nor write the data preparation software, but I participated in using the software to analyze cosmic ray results. In the thesis, the terms “clustering,” “local offset” and “relative local offset” are defined. Cosmic ray clustering was done in the data preparation software, but I redid the fit afterwards to explore sensitivity to the fit algorithm. With help from Dr. Lefebvre and Dr. Vachon, I helped design the software that calculated the relative local offsets from cosmic ray data. I wrote that software on my own. I was not involved in the design, data collection, data preparation or analysis of the x-ray data. I also was not involved in creating an alignment model from the x-ray data. I used the x-ray local offsets calculated using x-ray data analysis software to calculate relative local offsets with x-rays. I did the comparison between the x-ray and cosmic ray data.

I hereby declare that I am the sole author of this thesis. This is a true copy of the thesis, including any required final revisions, as accepted by my examiners.

¹⁴⁷

Chapter 1

¹⁴⁸

Introduction

¹⁴⁹ The Standard Model (SM) is a theoretical framework that describes experimental observa-
¹⁵⁰ tions of particles and their interactions at the smallest distance scales; however, the questions
¹⁵¹ the SM does not address motivate more experimentation.

¹⁵² Accelerators collide particles to generate interactions that can be recorded by detectors
¹⁵³ for further study. Detectors measure the trajectory and energy of all secondary particles
¹⁵⁴ produced in collisions to understand the interaction. The Large Hadron Collider (LHC) [1]
¹⁵⁵ at CERN is the world’s most energetic particle accelerator. Its energy makes it a unique
¹⁵⁶ tool to study elementary particles and their interactions in an environment with conditions
¹⁵⁷ similar to what would have existed in the early universe. If study at the energy frontier is
¹⁵⁸ to continue, the LHC must go on.

¹⁵⁹ After 2025, the statistical gain in running the LHC further without significant increase in
¹⁶⁰ beam intensity will become marginal. The High Luminosity Large Hadron Collider (HL-
¹⁶¹ LHC) project [2] is a series of upgrades to LHC infrastructure that will allow the LHC
¹⁶² to collect approximately ten times more data than in the initial design by \sim 2030. The
¹⁶³ increase in LHC beam intensity will result in a large increase in collision rate that will make
¹⁶⁴ accessible and improve statistics on several measurements of interest [3], many only possible
¹⁶⁵ at the LHC and the energy frontier. The increase in beam intensity will also increase the
¹⁶⁶ level of background radiation, requiring major upgrades to the experiments used to record
¹⁶⁷ the outcomes of the particle collisions.

¹⁶⁸ The ATLAS experiment [4] is one of the LHC’s general-purpose particle detector arrays, po-
¹⁶⁹ sitioned around one of the collision points of the LHC. During the 2019-2022 Long Shutdown
¹⁷⁰ of the LHC, the most complex upgrade of the ATLAS experiment is the replacement of the
¹⁷¹ small wheels of the muon spectrometer with the so-called New Small Wheels (NSWs) [5].

172 The detector upgrade addresses both the expected decrease in hit efficiency of the precision
173 tracking detectors and the high fake trigger rate expected in the muon spectrometer at the
174 HL-LHC. The NSWs are made of two different detector technologies: micromegas and small-
175 strip thin gap chambers (sTGCs). Micromegas are optimized for precision tracking while
176 sTGCs are optimized for rapid triggering, although each will provide complete coverage and
177 measurement redundancy over the area of the NSWs. Eight layers each of sTGCs cover the
178 NSWs. Practically, countries involved in detector constructor created quadruplet modules of
179 four sTGCs glued together that were arranged and installed over the area of the NSWs once
180 they arrived at CERN. Teams across three Canadian institutions built and characterized 1/4
181 of all the required sTGCs.

182 The sTGCs are gas ionization chambers that consist of a thin volume of gas held between two
183 cathode boards. One board is segmented into strip readout electrodes of 3.2 mm pitch. The
184 position of the particle track in the precision coordinate can be reconstructed from the strip
185 signals [5]. The sTGCs achieved the design track spatial resolution in the precision coordinate
186 of less than 100 μm per detector plane that will allow them to achieve a 1 mrad track angular
187 resolution using the 8 layers of sTGC on the NSW [6, 5]. The NSW measurement of the
188 muon track angle will be provided to the ATLAS trigger and used to reject tracks that do
189 not originate from the interaction point [5].

190 The precise measurement of a muon track angle depends on knowing the position of each
191 readout strip within the ATLAS coordinate system. To achieve this, the position of specific
192 locations on the surface of sTGC quadruplets will be monitored by the ATLAS alignment
193 system to account for time-dependent deformations [5]. Within a quadruplet module, the
194 strip positions could have been shifted off of nominal by non-conformities of the strip pattern
195 etched onto each cathode boards [7] and shifts between strip layers while gluing sTGCs into
196 quadruplets.

197 An xray gun was used to measure the offset of strips from their nominal position at the
198 locations that will be monitored by the ATLAS alignment system thereby providing, locally,
199 an absolute “as-built” strip position within the ATLAS coordinate system. Estimates of the
200 “as-built” positions of every readout strip are obtained by building an alignment model from
201 the available x-ray measurements [8].

202 The technique of measuring the “as-built” strip positions using xray data has never been
203 used before and must be validated. This thesis describes the use of cosmic muon data,
204 recorded to characterize the performance of each Canadian-made sTGC module, to validate
205 the x-ray strip position measurements. A description of how this work fits within the overall
206 alignment scheme of the NSW is also presented.

207 *Rewrite after implementing Brigitte’s edits.* Chapters 2 and 3 give more background on
208 particle physics, the LHC, ATLAS, the NSWs, and sTGCs. In chapter 4, the cosmic ray

209 testing procedure and how the position of the strips can be probed with cosmics data is
210 presented. Chapter 5 introduces the x-ray method, and in chapter 6, the x-ray offsets are
211 validated with cosmic muon data. The thesis concludes with a summary and outlook in
212 chapter 7.

²¹³ **Chapter 2**

²¹⁴ **High energy particle physics at the
LHC and the ATLAS experiment**

²¹⁶ Particle physics aims to study the elementary constituents of matter. Understanding the
²¹⁷ fundamental building blocks and how they interact provides insights into the evolution of
²¹⁸ the early universe to the forms of matter we observe today. This chapter introduces general
²¹⁹ concepts in particle physics relevant to understanding the physics goals of the HL-LHC and
²²⁰ NSW upgrade.

²²¹ The information on particle physics and the SM presented here is rather general; the reader
²²² is referred to [9, 10, 11] for more information.

²²³ **2.1 The Standard Model**

²²⁴ The Standard Model (SM) is the theoretical framework developed in the early 1970's to
²²⁵ describe the observed elementary particles and their interactions. It is built on a collection
²²⁶ of quantum field theories and has been remarkably successful at predicting experimental
²²⁷ observations, including but not limited to, the existence of the top quark [12], the tau
²²⁸ neutrino [13] and the Higgs boson [14, 15].

²²⁹ The known elementary particles described by the SM are represented in figure 2.1. There
²³⁰ are 12 matter particles (six quarks and six leptons), 4 force-mediating particles, and the
²³¹ Higgs boson. Each matter particle also has an anti-matter particle pair with the same
²³² mass but opposite charge, not represented in figure 2.1. The different forces of nature are
²³³ understood to be the result of the exchange of force-mediating particles between interacting

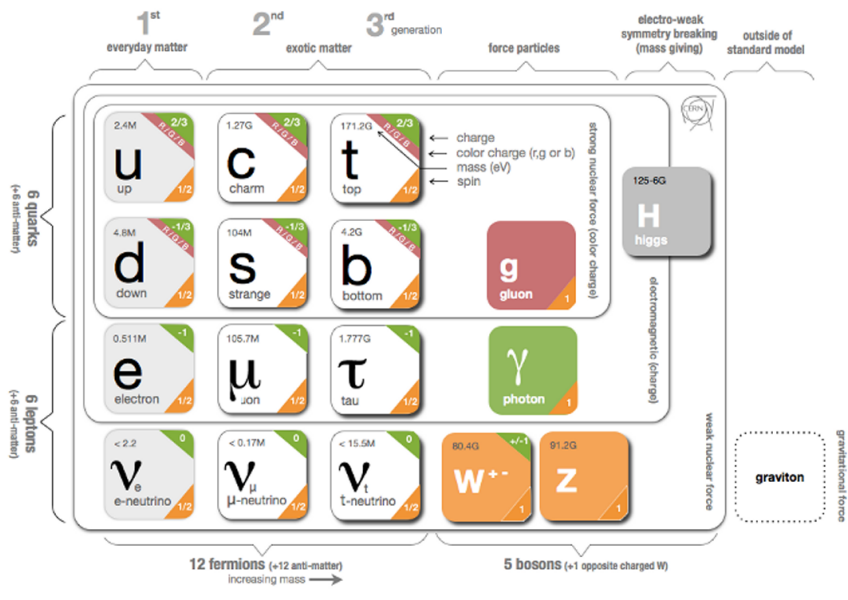


Figure 2.1: Schematic diagram of all elementary particles in the SM. Particles are grouped according to their properties and the forces through which they interact with other particles [16].

234 (coupled) particles. Photons are mediators of the electromagnetic force, W $+$ /- and Z bosons
235 are mediators of the weak force, and gluons are mediators of the strong force. At high
236 energy, the SM describes the electromagnetic and weak forces as stemming from a unified
237 electroweak force.. The Higgs boson field interacts with the particles mediating the unified
238 electroweak force to distinguish the weak and electromagnetic forces from each other at lower
239 energies and give particles (except neutrinos) a mass. This is called electroweak symmetry
240 breaking.

241 Quarks are matter particles that are sensitive to all forces; notably they are the only particles
242 sensitive to the strong force. Protons and neutrons are made up of quarks and gluons, and
243 the strong force is responsible for their existence and mutual attraction into nuclei [17].
244 Leptons are particles not sensitive to the strong force. Charged leptons include the electron,
245 which once part of atoms is responsible for chemistry. Of particular importance for this
246 thesis is the charged lepton called a muon. It is like the electron but its mass is \sim 200 times
247 larger than that of the electron. Muons have a lifetime of 2.2 μ s [11] and decay predominantly
248 as $\mu \rightarrow e^- \bar{\nu}_e \nu_\mu$. Neutrinos are neutral, almost massless leptons that only interact through
249 the weak force.

250 Common matter is made up of the lightest constituents of the SM: up and down quarks,
251 electrons and photons. The other particles are produced in high-energy environments but
252 then decay to the lightest constituents. Such high energy environments include the conditions
253 present in the early universe [18], astrophysical sources, and particle accelerators. The
254 presence of the particles of the SM at the beginning of the Universe means that their interactions
255 and decays are fundamental for the study of the evolution of the early universe [18].
256 Many high energy astrophysical sources, like supernovae, generate particles that rain down
257 on Earth as cosmic rays [19]. Particle accelerators have been built to create controlled environments
258 of high-rate particle collisions at high energy where the production and decay of
259 elementary particles can be directly studied..

260 2.2 Beyond the Standard Model

261 Despite its success at describing most experimental observations to date, there is ample
262 evidence that the SM is not a complete description of natural phenomena at the smallest
263 scales. For example, the SM has a large number of free parameters, the values of which have
264 to be fine-tuned to fit experimental observations. This is part of the so-called “naturalness”
265 problem.

266 Furthermore, the SM provides no explanation for several open questions in particle physics.
267 First, neutrinos in the SM are assumed to be massless and do not gain mass in the same way

as the other particles. However, in 2013 neutrino were confirmed to change between their different flavours [20], which can only occur if neutrinos do have mass [21]. The neutrino mass requires physics beyond the standard model [22]. Second, several astrophysical and cosmological measurements suggest the presence of “dark matter” making up 85 % of the matter content of the universe [23]. The nature of dark matter is unknown and so far there is no SM explanation [24]. Third, the SM does not explain the origin and nature of the matter- antimatter asymmetry that produced our matter-dominated universe. Finally, the SM does not include a description of gravity.

Theoretical extensions beyond the Standard Model (BSM) aim to address some of these questions, often predicting existence of yet-unseen elementary particles and/or physics phenomena beyond those predicted by the SM. For example, super-symmetry (SUSY) predicts that each SM particle has a heavier super-symmetric partner. SUSY would explain the origin of dark matter with weakly interacting massive particles, would solve the so-called “naturalness” problem in the SM [25]. These hypothetical new physics phenomena and/or new particles can be searched for at particle accelerators.

2.3 Studying high energy particle physics with accelerators

In particular, particle accelerators of increasingly higher energy have a long history of enabling the discovery of predicted, yet-unseen particles. These include, for example, the discovery of the W [26, 27] and Z bosons [28, 29], the top quark [30, 31], and most recently, the discovery of the Higgs boson [32, 33] marking the completion of the SM as it is known today.

Based on the established success of the SM, there are two approaches to particle physics research. One approach is to search for the existence of new physics phenomena predicted to exist in BSM theories and the other is to test the validity of the SM to a high degree of accuracy to search for flaws in the model. Standard Model predictions are generally expressed in terms of the probability of a specific physics process to occur, expressed as a cross section in units of barns (with 1 barn = 10^{-28} m²). As an example, figure 2.1 shows a summary of cross section measured for different physics processes using the ATLAS experiment and their comparison with the predictions of the SM. Most cross section measurements agree well within one standard deviation with the SM predictions.

Particle accelerators provide a controlled and high-collision rate environment that makes them ideal places to search for new physics phenomena and to carry out systematic tests of

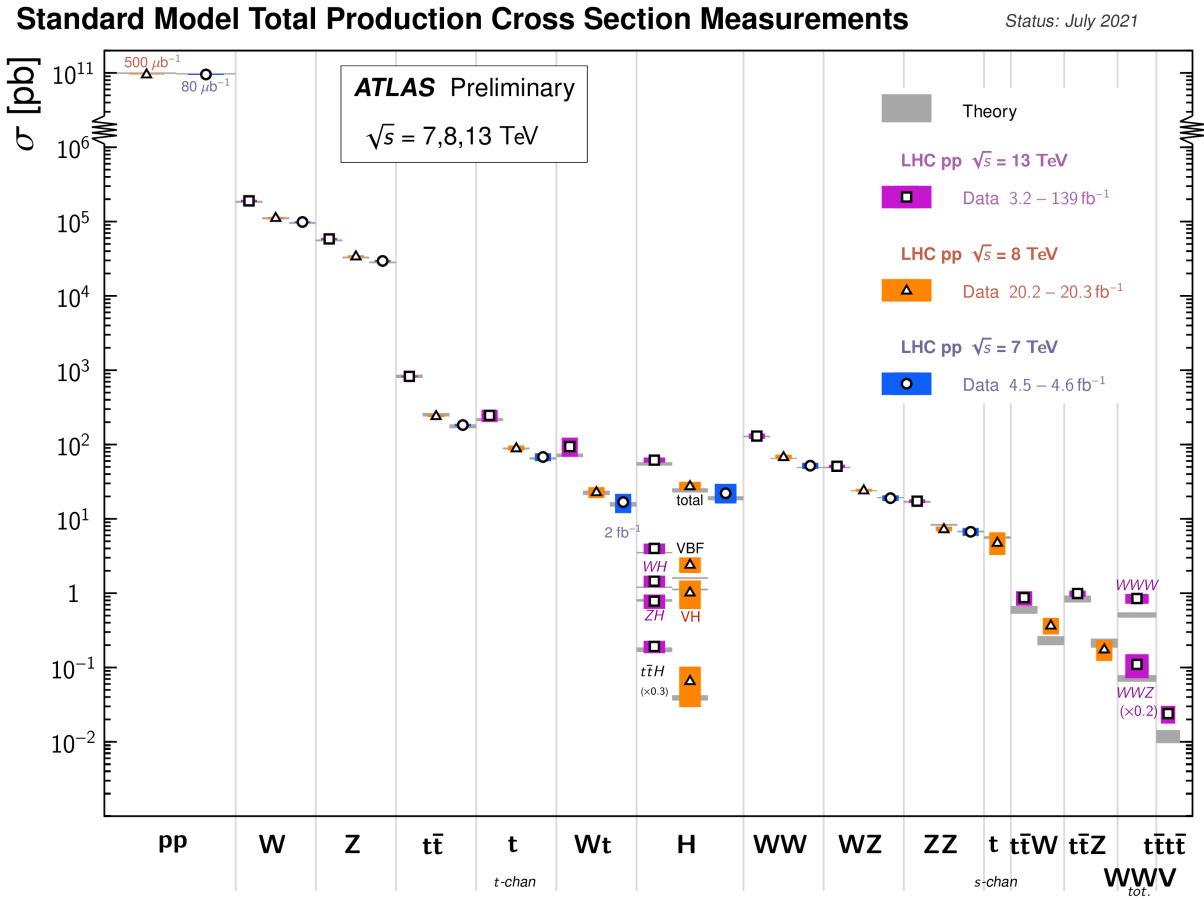


Figure 2.2: Production cross sections of different final states measured by the ATLAS experiment at the LHC. Comparison with the SM theory predictions is also shown [34].

301 the SM. The LHC is the highest energy collider in the world so it can access physics that no
302 other accelerator can, notably the direct production of the Higgs boson and top quark. A
303 description of the LHC and the ATLAS detector are provided in the next chapter.

304 2.4 The Large Hadron Collider

305 The LHC is an accelerator 27 km in circumference and located \sim 100 m underground at
306 CERN near Geneva, Switzerland [1]. It has two beam pipes that counter-circulate bunches
307 of protons¹ before colliding the bunches in the center of one of four major experiments, such
308 as the ATLAS experiment (discussed in section 2.7). In the previous run of the LHC (run-2),
309 protons were collided with a center of mass energy of 13 TeV. It is not actually the protons
310 that interact, but the constituent quarks and gluons (partons) that each carry some fraction
311 of the energy and momentum of the collisions.

312 2.5 Luminosity

313 The number of proton-proton interactions generated by the LHC directly affects the statis-
314 tics available to make measurements of cross sections, SM parameters, etc. Predicting the
315 number of proton-proton interactions requires defining a metric called luminosity [11]. It is
316 the number of particles an accelerator can send through a given area per unit time. It is
317 calculated from the measurable quantities in equation 2.1:

$$\mathcal{L} = \frac{f N_1 N_2}{4\pi\sigma_x\sigma_y} \quad (2.1)$$

318 f is the frequency of the bunch crossings (25 ns), N_1 and N_2 are the number of protons in
319 each bunch ($\sim 10^{11}$ protons / bunch), and σ_x and σ_y are the RMS of the spatial distributions
320 of the bunch. Therefore, luminosity is a property of accelerator beams, which are set by the
321 capabilities of the accelerator. The design luminosity of the LHC was 10^{34} cm $^{-2}$ s $^{-1}$. The
322 units of luminosity are an inverse area; multiplying the luminosity by the cross section of a
323 given process gives the expected rate for that process.

324¹the LHC also accelerates lead ions, but ATLAS is best at recording proton-proton collisions. The ALICE
325 experiment [35] was designed for lead-lead interactions.

324 Integrating the *instantaneous* luminosity (equation 2.1) over a period of data collection gives
325 the integrated luminosity,

$$L = \int \mathcal{L}(t) dt \quad (2.2)$$

326 which is related to the total number of interactions. In this way, the luminosity is the link
327 between the accelerator and the statistical power of measurements to be made with the data
328 collected. So far, the LHC provided an integrated luminosity of 28.26 fb^{-1} in run-1 [36] and
329 156 fb^{-1} in run-2 [37].

330 2.6 The High-luminosity LHC

331 The HL-LHC upgrade [2] was accepted because without increasing the luminosity of the LHC
332 tenfold, running the accelerator will not provide significant statistical gain on measurements.
333 Also, some systems will need repair and replacement to operate past ~ 2020 . The LHC will
334 be the most energetic accelerator in the world for years to come and is the only accelerator
335 capable of directly producing the Higgs boson (and top quarks), so the European Strategy for
336 Particle Physics made it a priority “to fully exploit the physics potential of the LHC” with
337 “a major luminosity upgrade” [38]. The goal is for the HL-LHC to provide an integrated
338 luminosity of 3000 fb^{-1} in the 12 years following the upgrade. The luminosity actually
339 achieved will depend on a combination of technological advances and upgrades in progress
340 that affect the factors contributing to luminosity defined in equation 2.1 [2].

341 The most anticipated measurement at the HL-LHC is of the triple-Higgs coupling. Measuring
342 the coupling allows the shape of the Higgs potential responsible for electroweak symmetry
343 breaking to be measured. Any discrepancy with the SM prediction will show that there
344 must be other sources of electroweak symmetry breaking, and hence currently unpredicted
345 particles. The LHC is the only accelerator where the Higgs can be produced directly and
346 the HL-LHC upgrade is required to have sufficient di-Higgs production to make a meaning-
347 ful measurement [3, 40]. Accordingly, detector sensitivity to various Higgs decays will be
348 important at the HL-LHC.

349 2.7 The ATLAS experiment

350 The ATLAS experiment [4] was designed to support all the physics goals of the LHC. It is
351 44 m long and 25 m in diameter, and weighs 7000 tones. It is an array of particle detector



Figure 2.3: LHC/HL-LHC plan [39]. The integrated luminosities collected and projected for each run of the LHC are shown in blue boxes below the timeline and the center of mass energy of the collisions is shown in red above the timeline. The top blue arrow labels the run number. “LS” stands for “long shutdown” and indicates periods where the accelerator is not operating. During the shutdowns, upgrades to the LHC and the experiments are being installed. This timeline was last updated in January, 2021, and reflects changes in the schedule due to the ongoing pandemic.

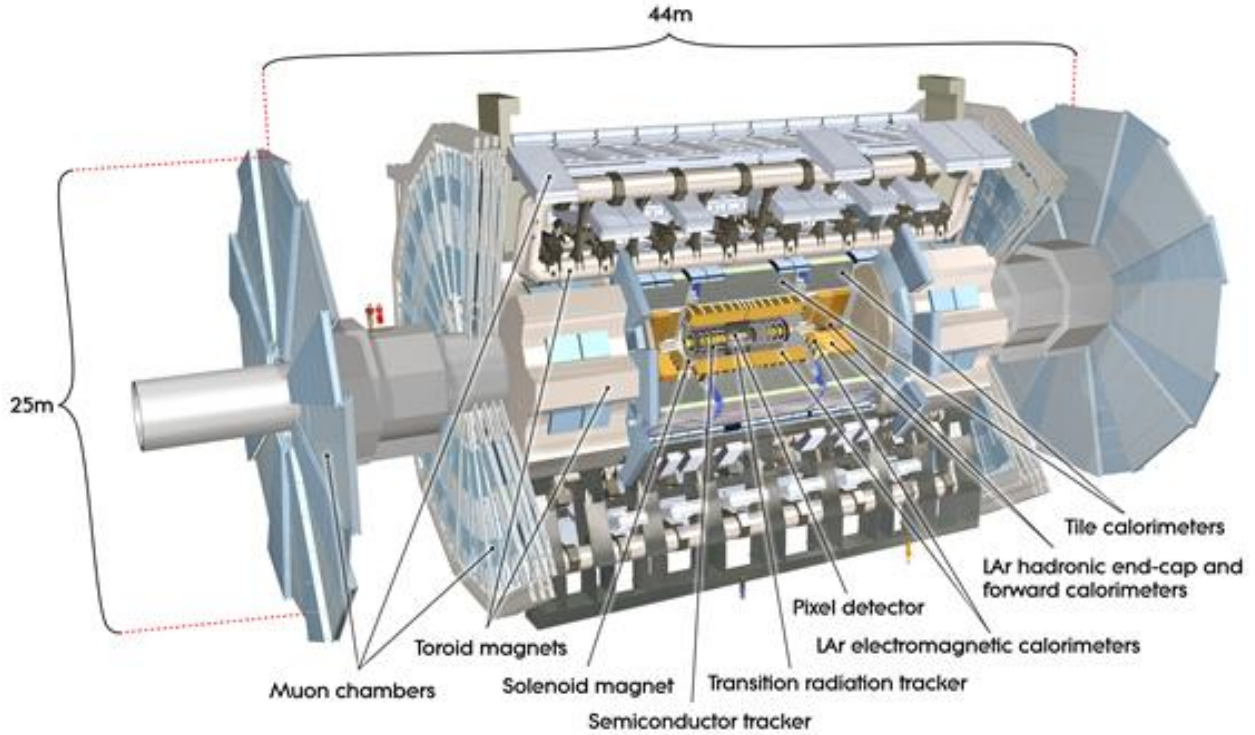


Figure 2.4: Diagram of the ATLAS experiment, with the various detector subsystems labelled [4].

352 subsystems arranged concentrically around the beam pipe and centered around one of the
 353 LHC’s interaction points (a place where the beams collide), as shown in figure 2.4. ATLAS is
 354 cylindrical because it aims to provide 4π coverage around the interaction point. It is helpful
 355 to separate the subsystems of ATLAS into the so-called “barrel” and “endcap” / “forward”
 356 regions, referring to the cylindrical geometry.

357 For analysis, ATLAS is typically described in spherical coordinates. The azimuthal angle
 358 ϕ is measured around the beampipe and the polar angle θ is measured from the beam
 359 pipe. A more useful coordinate than θ is the pseudo-rapidity, $\eta = -\ln \tan(\theta/2)$, because
 360 it approaches the rapidity of a particle when its momentum is much greater than its mass
 361 and differences in rapidity are approximately invariant to a Lorentz boost parallel to the
 362 beam. The range of η is 0 (perpendicular to the beam) to $\pm\infty$ (parallel to the beam, or the
 363 z-direction). Typically, η is the physically interesting coordinate because the ϕ coordinate
 364 follows the cylindrical symmetry of the beam.

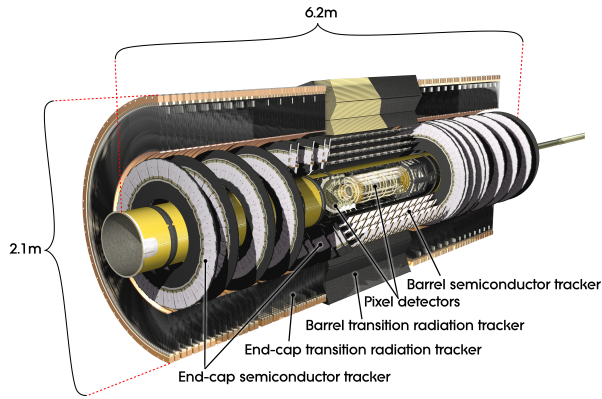


Figure 2.5: Diagram of the ATLAS experiment’s inner detector, with the different segments and the technology used labelled [4].

365 ATLAS provides identification and kinematic measurements for each particle created after
 366 the initial collision. Predictions made using SM and BSM theories can then be compared
 367 to the data. Each subsystem of ATLAS collects certain information and a complete
 368 description of each recorded collision can be assembled offline. An overview of the main
 369 ATLAS subsystems is given below.

370 **The inner detector**

371 The inner detector [41, 42] (figure 2.5) is for precision tracking, vertex measurements and
 372 electron identification. A 2 T solenoid with field parallel to the beam bends the track of
 373 outgoing particles. The innermost part is made of high-resolution semiconductor pixel and
 374 strip detectors while the outermost part are straw-tubes that generate and detect transition
 375 radiation

376 **Calorimetry system**

377 Electromagnetic and hadronic sampling calorimeter units are used to record the energy
 378 of electrons, photons and jets. A combination of liquid-argon (LAr) electromagnetic and
 379 hadronic calorimeters [43] and tile-scintillator hadronic calorimeters [44] cover the rapidity
 380 range $|\eta| < 4.9$, as shown in figure 2.6.

381 The calorimeters cause incoming charged particles to shower and deposit their energy in
 382 the sensitive volume. Only muons and neutrinos are known to pass the calorimeters to the
 383 muon spectrometer. Particles other than those mentioned would have decayed in the inner
 384 detector before reaching the calorimeter.

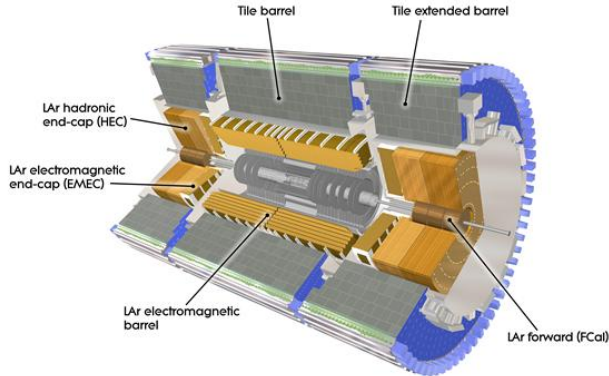


Figure 2.6: Diagram of the ATLAS calorimeter system, with the different segments and the technology used labelled [4].

385 Trigger system

386 It would be impossible to record all the data from bunch crossings every 25 ns, corresponding
 387 to a rate of ~ 40 MHz. ATLAS has a multi-level trigger system to select events of interest
 388 for permanent storage. The Level-1 (L1) hardware trigger [45] uses partial-granularity infor-
 389 mation from the muon spectrometer and calorimeter to trigger on high p_T muons, electrons,
 390 jets, high missing transverse energy, and τ decaying to hadrons. The maximum L1 trigger
 391 rate ATLAS can accommodate is 100 kHz with a latency of 2.5 μ s. After run-3 an upgrade
 392 of the trigger system will allow for a higher rate and more latency, but for now these are the
 393 working limits [46].

394 The L1 trigger is used to define regions of interest that are fed into the software high level
 395 trigger (HLT), in which the full granularity of the muon spectrometer and calorimeter are
 396 used with information from the inner detector to reduce the trigger rate to 1 kHz. Events
 397 that pass the L1 and HLT trigger are recorded for use in offline analysis [47].

398 The ATLAS trigger system is described in the references above but the trigger rates quoted
 399 here are after the upgrades implemented for run-2, described in [48].

400 Muon spectrometer

401 The muon spectrometer has multiple layers, each of which records the position of a pass-
 402 ing muon. Magnetic deflection by superconducting air-core toroid magnets bend the muon
 403 tracks. The position information recorded in each layer and the magnetic field are used to
 404 reconstruct each muon's momentum. In the barrel of ATLAS, eight coils bent into “race-
 405 tracks” arranged around the beampipe provide the magentic field. In the forward region,

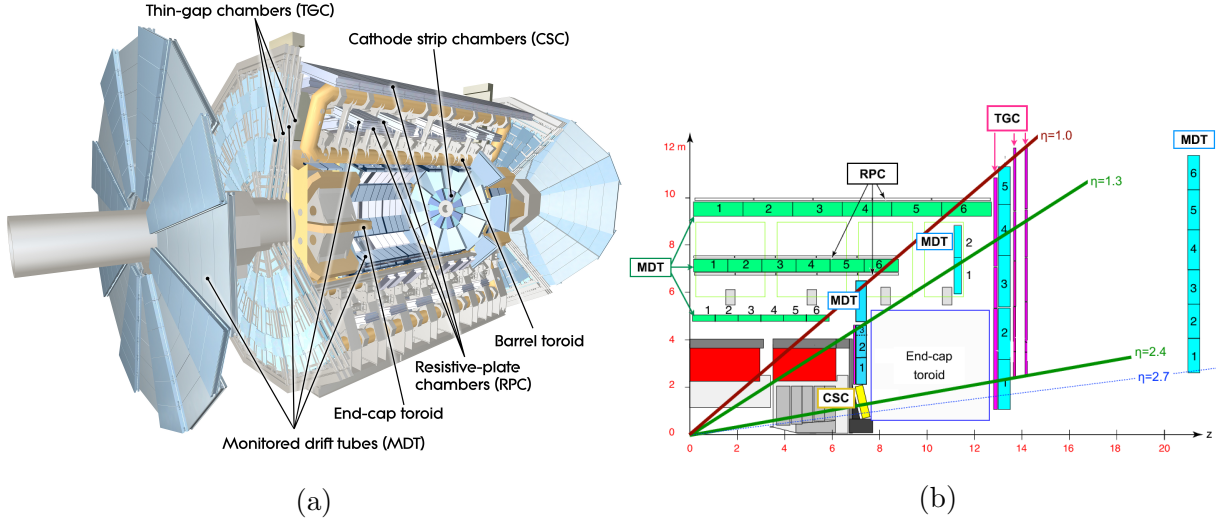


Figure 2.7: (a) The ATLAS muon spectrometer [4]. (b) A quarter-cut of ATLAS, with the interaction point in the bottom left corner. The small wheel is just left of the end cap toroid, the big wheel is to its right, and the outer wheel is the rightmost structure [50].

406 two end-cap toroids each with eight smaller racetrack-shaped coils arranged symmetrically
 407 around the beampipe are inserted in the ends of the barrel toroid [49]. Figure 2.7 shows the
 408 toroid magnets and the different parts of the ATLAS muon spectrometer [4].
 409 The muon spectrometer [51] is separated into detectors used for precision offline tracking
 410 and for triggering. Three layers of monitored drift tubes (MDTs) or cathode strip chambers
 411 (CSCs) are used for tracking. The position of the muon track in each of the three layers allows
 412 reconstruction of the track and hence momentum. For the design momentum resolution of
 413 $\Delta p_T/p_T < 1 \times 10^{-4} p / \text{GeV}$ for $p_T < 300 \text{ GeV}$ and a few percent for lower p_T muons,
 414 the MDTs and CSCs required position resolution of $50 \mu\text{m}$ each. Accordingly, an optical
 415 alignment system was designed to monitor and correct for chamber positions [51, 52].
 416 Resistive plate chambers (RPCs) are used for triggering in the barrel and thin-gap chambers
 417 (TGCs) are used for triggering in the endcaps. The positions of each type of chamber are
 418 sketched in figure 2.7b. Often, the endcap muon spectrometer is separated into three wheels –
 419 the small wheel, big wheel, and outer wheel – ordered by proximity to the interaction point.
 420 In run-1, low (high) p_T muons were triggered on at L1 if two (three) of the RPCs or TGCs
 421 layers around the big wheel fired in coincidence, for the barrel and endcaps respectively [45].
 422 After run-1 it was discovered that up to 90% of the triggers in the endcap were fake, caused
 423 by background particles generated in the material between the small wheel and the big
 424 wheel [5]. To reduce the fake rate in run-2, the TGCs on the inside of the small wheel also

425 had to register a hit. The added condition reduced the trigger rate by 50% in the range 1.3
426 $< |\eta| < 1.9$ [48]. The effectiveness of the solution was limited since the $|\eta|$ -range of the small
427 wheel TGCs was limited to $1.0 < |\eta| < 1.9$ and the position resolution of the small wheel
428 TGCs is coarse [5].

429 **Chapter 3**

430 **The New Small Wheels**

431 **3.1 Motivation for the New Small Wheels (NSWs)**

432 The hit rate of all detector systems will increase with the HL-LHC not only because of the in-
433 crease in luminosity, but also because the background radiation rate increases proportionally
434 with luminosity. The combined rate presents problems for both the tracking and triggering
435 capabilities of the muon spectrometer [5].

436 In term of tracking, the efficiency of the MDTs decreases by 35% (mostly due to long dead-
437 times) already when exposed to the maximum hit rate at the current luminosity, 300 kHz.
438 At the threefold increase in luminosity predicted for run-3, most of the small wheel will be
439 subjected to a hit rate well above 300 kHz and it will begin missing hits. Losing hits in the
440 small wheel will reduce the high p_T muon momentum resolution. The decrease in resolution
441 will affect the ability to search for, for example, the decay of heavy bosons (W' , Z') or a
442 pseudo-scalar Higgs predicted by some SUSY models [3].

443 Already, the forward muon trigger system copes with a very high fake rate, even when
444 including TGC data from the small wheel in the trigger as in run-2. At the luminosity
445 expected in run-3, 60 kHz of the maximum 100 kHz of the L1 trigger would be taken by the
446 endcap muon spectrometer. A possible solution would be to raise the minimum p_T threshold
447 from 20 GeV to 40 GeV, but the ability to study several physics processes of interest depend
448 on low p_T muons, particularly the Higgs decay to two muons, the Higgs decay to two tau's
449 and SUSY particle decays to leptons [5].

450 The NSWs will solve both these problems. It will be covered with precision tracking cham-
451 bers suitable for the expected hit rates and triggering chambers capable of 1 mrad angular



Figure 3.1: A schematic of a quarter cross section of the ATLAS detector, with the collision/interaction point (IP) in the bottom left corner. Three possible tracks are labelled. Ideally, track A would be triggered on while track B and C discarded. With the small wheel, all three tracks would be recorded. With the NSW, only track A would be recorded [5].

resolution. The idea behind the triggering chambers is to match the small wheel track segment with the track segment from the big wheel to discard tracks not originating from the interaction point. Figure 3.1 illustrates this point: the run-1 trigger system would have triggered on all three tracks, while with the NSW the trigger system would only trigger on track A. Reducing the fake trigger rate means the NSWs will not miss as many muon hits and that the low p_T threshold will not have to be raised to cut particles not produced in the collision. The NSWs allow ATLAS to maintain the high p_T muon resolution and the low muon p_T threshold at the HL-LHC collision rate [5].

460 **3.2 Design of the NSWs**

461 The NSWs are covered with two detector technologies: micromegas and small-strip thin gap
462 chambers. MMs are the primary tracking detectors and sTGCs are the primary triggering
463 detectors, but for redundancy sake both are designed to do either. Both sets of detectors are
464 to have position resolution better than $\sim 100 \mu\text{m}$ per plane. Four chambers of each type are
465 glued together to create quadruplet modules. Quadruplets of different sizes are assembled
466 into wedges. Two sTGC wedges and two MM wedges are layered to create sectors (with
467 the sTGC wedges on the outside) [5]. Different stages of the construction process are shown
468 in figure 3.2. At the time of writing, both NSWs have been assembled. The first has been
469 lowered into the ATLAS cavern and is being commissioned. The second will be lowered
470 shortly.



(a) An sTGC quadruplet module. The left image highlights the trapezoidal shape. The right image shows the short edge corner. The four sTGC layers and each layer's gas inlet are visible. The gas outlets and high voltage cables are at the long edge in the back of the photo. The green printed circuit board along the sides are the adaptor boards where the front end electronics are attached.



(b) Left: An sTGC wedge. The white frame outlines the individual quadruplet modules. Right: A completed sector, with two sTGC wedges on the outside and two MM wedges on the inside.



(c) The New Small Wheel. All sectors except one large sector at the top are installed, revealing two of the smaller sectors that are normally hidden under the large sectors and support bars. The NSWs are 10 m in diameter.

Figure 3.2: Images breaking down some of the construction units of the NSWs.



Figure 3.3: Internal structure of an sTGC, zoomed into the area under a pad. High voltage is applied to wires suspended in the gas volume to create an electric field. A passing muon causes an ionization avalanche that is picked up by the wire, strip and pad electrodes [8].

⁴⁷¹ 3.3 Small-strip thin gap chambers

⁴⁷² sTGCs are gas ionization chambers operated with a CO₂:n-pentane ratio of 55:45. Gold-
⁴⁷³ plated tungsten wires, 50 µm in diameter and with 1.8 mm pitch, are suspended between
⁴⁷⁴ two cathode planes made of FR-4, each 1.4 mm away (see figure 3.3). One cathode board is
⁴⁷⁵ segmented into pads of varying area (around 300 cm² each), and the other segmented into
⁴⁷⁶ strips of 3.2 mm pitch, perpendicular to the wires. High voltage is applied to the wires and
⁴⁷⁷ the cathode planes are grounded [5, 53]. When a muon passes through, the gas is ionized
⁴⁷⁸ and the electric field in the gas gap causes an ionization avalanche [54]. The motion of the
⁴⁷⁹ ions and electrons are picked up on the nearby wire, strip and pad electrodes [5]. The gas
⁴⁸⁰ mixture was chosen to absorb excess photons produced in the avalanche that delocalize the
⁴⁸¹ avalanche signal [55]. The resistivity of the carbon coating and capacitance of the pre-preg

sheet tune the spread of the charge distribution [56] and the speed of the response [57] to optimize the rate capability. The hatching of the strips and wires establishes a coordinate system from which to extract the coordinate of the muon as it passes through the chamber. The small pitch of the strips is what allows the quadruplets to deliver good angular resolution to improve the fake trigger rate and meet the precision tracking requirements [5].

A 3-out-of-4 coincidence in pad electrodes from each layer of a quadruplet define a region of interest where the strip and wire electrodes should be readout. The pad triggering scheme greatly reduces the number of electrodes that require read-out so that a track segment of the required angular resolution can be provided quickly enough to the hardware trigger [5].

Signal is readout from groups of successive wires, so the position resolution in the direction perpendicular to the wires is 10 mm. The wires give the symmetric azimuthal coordinate in ATLAS so the position resolution in this direction is sufficient. Good resolution on the η coordinate, perpendicular to the strips, is important [5]. The average single chamber position resolution in the strip coordinate was 45 μm for perpendicular muon tracks as measured in a test beam [6] – well within design specifications. When four sTGCs are glued together into a quadruplet the design angular resolution of 1 mrad in the strip coordinate is achievable [5, 53].

Therefore, sTGCs are able to meet the triggering and precision tracking goals they were designed for. To ensure they can deliver once installed in ATLAS, knowing the position of the strips to within their position resolution in the ATLAS coordinate system is necessary. The NSW alignment system, detailed in section 3.5, monitors the position of alignment platforms installed on the surface of the wedges. The alignment platforms are installed with respect to an external reference on the sTGCs: two brass inserts on each strip layer on one of the angled sides of each quadruplet (shown in figure 3.4). So the challenge of positioning the strips in ATLAS was separated into two steps: first, position the strips with respect to the brass inserts; second use the alignment system to position the alignment platforms. The next section provides some pertinent details on the sTGC construction process, with steps that affect the position of the strips with respect to the brass inserts highlighted.

3.4 sTGC Quadruplet Construction

Five countries were responsible for producing the sTGC modules of varying geometries for the NSW: Canada, Chile, China, Israel and Russia. Canada was responsible for 1/4 of the required sTGCs, of three different quadruplet geometries. The steps of the construction process in each country were similar [5]. The process followed in Canada is detailed.

TRIUMF in Vancouver, British Columbia was responsible for preparing the cathode boards. The boards were made and the electrodes etched on at a commercial laboratory, Triangle



(a) Brass insert near long edge.

(b) Brass insert near short edge.

Figure 3.4: The brass inserts sticking out from the gas volumes of an sTGC quadruplet. These inserts were pressed against alignment pins when the individual sTGCs were being glued together.

516 Labs, in Carson City, Nevada. Once completed they were sent to TRIUMF to be sprayed with
517 graphite and otherwise prepared [7]. The boards are commercial multilayer printed circuit
518 boards, but the strip boards required precision machining to etch the strip pattern [5].
519 Triangle Labs also machined the two brass inserts into each strip board. A coordinate
520 measuring machine (CMM) was used to digitize a set of reference strips. Four quality
521 parameters describing non-conformities in the strip pattern of each board with respect to
522 the brass inserts were derived from the data and the results are available on a QA/QC
523 database. The parameters and the CMM data collection is described in full in [7]. Due to
524 time constraints, tolerances on the non-conformities in the etched strip pattern with respect
525 to the brass inserts were loosened, with the condition that the strip positions in ATLAS
526 would have to be corrected for [7].

527 The prepared boards were sent to Carleton University in Ottawa, Ontario for construction
528 into sTGCs and quadruplets. First, the wires were wound around the pad cathode boards
529 using a rotating table and the wires were soldered into place. A wound pad cathode board
530 was held by vacuum on a granite table, flat to within 20 μm , and a strip cathode board glued
531 on top to create an sTGC. Holding one sTGC flat with the vacuum, another was glued on
532 top to create a doublet, then two doublets were glued together to create a quadruplet. When
533 gluing sTGCs together, the brass inserts were pushed against alignment pins with the goal of
534 keeping the strip layers aligned within tolerance. However, non-conformities in the shape of
535 the brass inserts, non-conformities in the position of the alignment pins and shifts between
536 sTGCs while the glue cured resulted in misalignments between the brass inserts and strip
537 layers. Precise alignment of the pad boards or wires with respect to the strip boards did not
538 have to be so tightly controlled because pads do not measure the precision coordinate.

539 The Carleton team finished the quadruplets by installing adaptor boards on the angled sides
540 of each layer that allow front end electronics to be attached. Completed quadruplets were
541 sent to McGill University where they were characterized with cosmic rays. The details of
542 cosmic ray testing are described in chapter 4. Tested quadruplets were sent to CERN where
543 they were assembled into wedges and alignment platforms installed. The alignment platforms
544 were installed using a jig positioned with respect to the brass inserts. Completed wedges
545 were assembled into sectors then installed on the NSWs.

546 The quadruplet construction process had two steps where strip positions could be shifted off
547 of nominal. At board-level, there could be non-conformities in the etched strip pattern with
548 respect to the brass inserts, described by the four quality parameters [7]. At the quadruplet
549 level, misalignments between the brass inserts and strips on different layers were introduced
550 during the gluing. The result was that the brass inserts were not a reliable reference point
551 and that the strips can be offset from their design position by up to hundreds of micrometers.
552 Offsets in strip positions from nominal in Canadian quadruplets were shown to be random [7],

so no one correction would suffice. The offsets must be measured and corrected for in the ATLAS offline software that does the precision tracking. Understanding the work ongoing to make measurements of offsets and correct for them requires understanding the strategy of the NSW alignment system.

3.5 NSW alignment

The idea of the NSW alignment system is presented in [5], but the details have only been presented internally so far. After the wedges are constructed, alignment platforms are installed on every sTGC quadruplet and optical fibres routed to them, as shown in figure 3.5. Light from the optical fibres will be monitored in real time by cameras (BCAMs) mounted on the alignment bars of the NSWs. The system will thus record the positions of the alignment platforms in the ATLAS coordinate system, accessible at any point during operation.

The original alignment scheme was to use the brass inserts as a reference between the alignment platforms and the individual strips, as shown in the solid arrows in figure 3.6 – this will no longer work. The position of the alignment platforms will be known thanks to the alignment system, so a different method to get the position of the strips with respect to the alignment platforms is currently in its final stages. It uses the yet-unmentioned x-ray dataset to calculate offsets of the strip pattern of an sTGC layer in a local area (local offset) with respect to the nominal geometry by analyzing the beam profile left by an x-ray gun attached to different positions on the alignment platforms. Effectively, the reference to the brass inserts is skipped, represented as the dashed line in figure 3.6. The alignment platforms provide the link to the nominal geometry because their position with respect to the strips can be calculated from the nominal geometric parameters assuming that the strips are perfectly etched and aligned. Cosmic muon track positions cannot be compared to the nominal geometry because the alignment platforms are not installed when cosmics data is collected, so there is no external reference to provide a link to the nominal geometry.

The x-ray method does not have the sensitivity to measure the offset of each strip from nominal, but instead the offset of the strip pattern in a local area around the position of the gun can be measured. *Local offsets* are used to build an alignment model for each strip layer. Formally defined, an alignment model is a set of parameters used to estimate the true position of a strip given its nominal position. The alignment model currently being worked on takes x-ray and CMM data as input to calculate an offset and rotation of each strip layer with respect to nominal [8]. The alignment parameters could be described as “global”, meaning over the whole layer instead of local. Without the x-ray dataset, there would be no input to the alignment model that takes into account inter-layer misalignments introduced

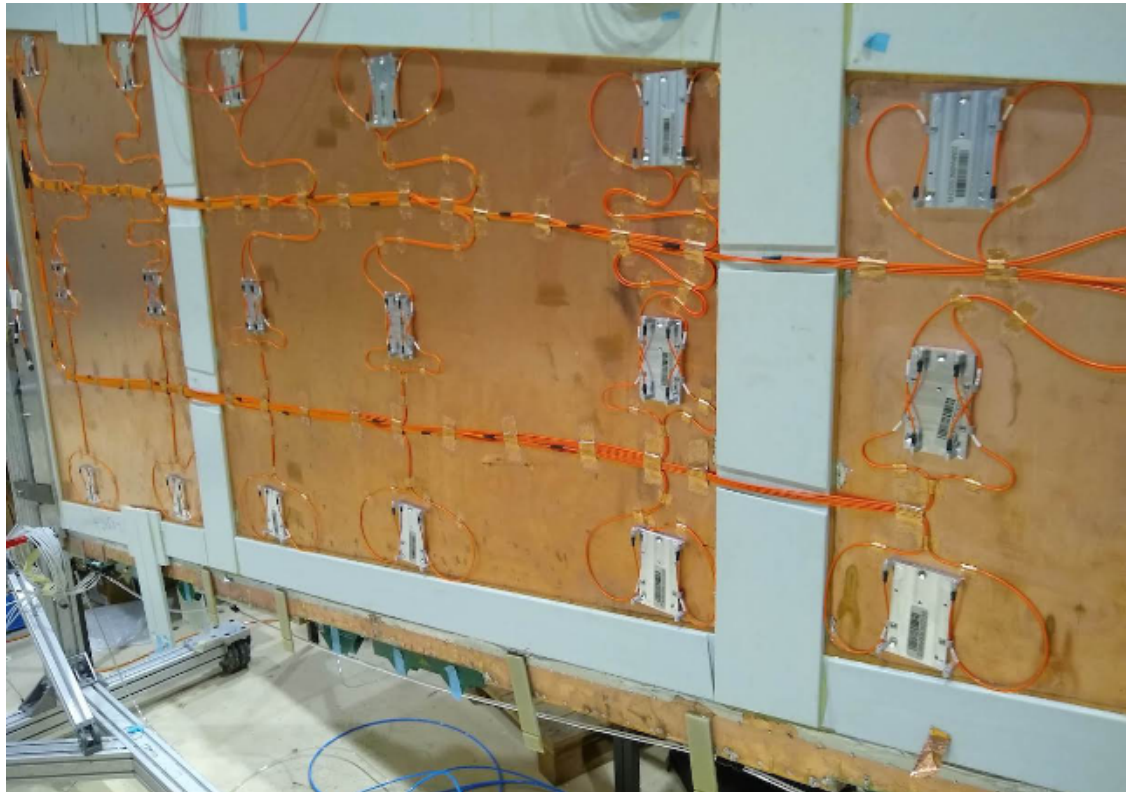


Figure 3.5: An sTGC wedge with alignment platforms (silver) installed on the quadruplet. Optical fibres (orange) are routed to the alignment platforms. Cameras on the frames of the NSWs will record light from the optical fibres to position the alignment platforms in the ATLAS coordinate system.

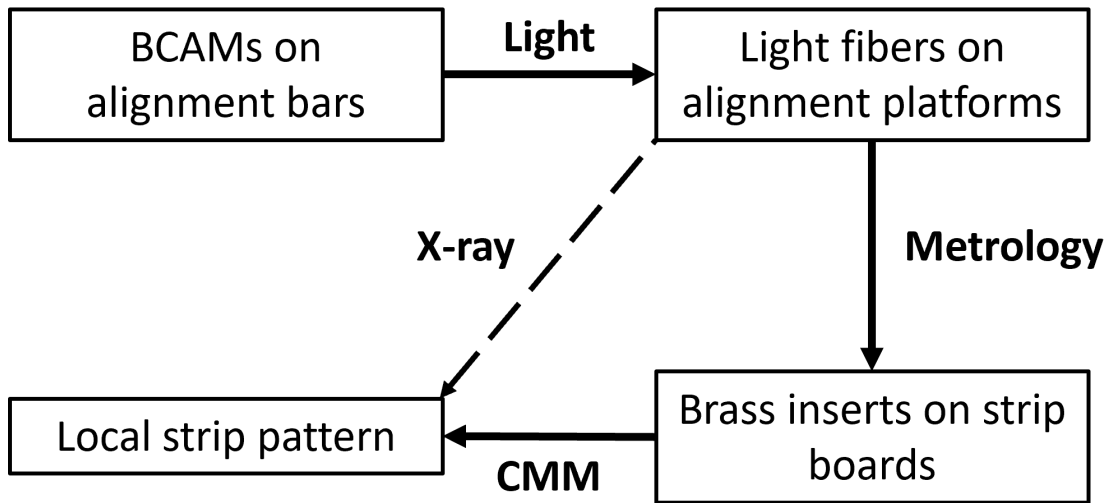


Figure 3.6: How the different elements of the sTGC alignment system relate to one another. The solid arrows denote the planned alignment scheme. The dashed arrow shows the modification being finalized now. This figure was originally designed by Dr. Benoit Lefebvre.

⁵⁸⁷ in construction.

⁵⁸⁸ Given that the x-ray local offsets can only be measured at positions where the gun can be
⁵⁸⁹ attached and that they are an important part of the alignment scheme, the x-ray method
⁵⁹⁰ needs to be validated. The goal of this thesis is to validate the x-ray local offsets while
⁵⁹¹ exploring how cosmics data complements and adds to the understanding of strip positions
⁵⁹² and overall alignment.

593 **Chapter 4**

594 **Using cosmic muons to measure
595 relative strip position offsets**

596 At McGill, among other quality and functionality tests, each Canadian-made quadruplet was
597 characterized with cosmic muons. In this chapter, the experimental setup and how the data
598 was analyzed to provide relative strip position offsets is presented. The analysis method
599 was motivated by the how it could be compared to data collected with the x-ray method
600 (chapter 5) but also stands alone as a characterization of the alignment between strips of
601 different layers. First, a brief introduction to cosmic rays.

602 **4.1 Cosmic rays**

603 The Earth is being bombarded by particles from the sun, galactic sources and extra galactic
604 sources – collectively called cosmic rays [19, 11]. Cosmic rays are mostly protons, but also
605 heavier ions, gamma rays and the term sometimes includes neutrinos. The primary (initial)
606 cosmic ray interacts with the atmosphere causes electromagnetic and hadronic showers of
607 particles. Hadronic showers result from the primary cosmic ray interacting strongly with the
608 target of the atmosphere and the most abundant products are pions. Charge pions mostly
609 decay to muons (there is a lesser contribution to the muon flux from kaons as well) [58].
610 Thanks to time dilation extending the muon’s lifetime as measured on Earth, a flux of
611 approximately 1 muon/cm²/ min reaches the ground [11]. Measuring the muon flux and
612 energy spectrum reveals information about primary cosmic rays [58] which is interesting to
613 high energy physicists and astrophysicists. The muon flux is also terribly convenient for
614 testing muon detectors.

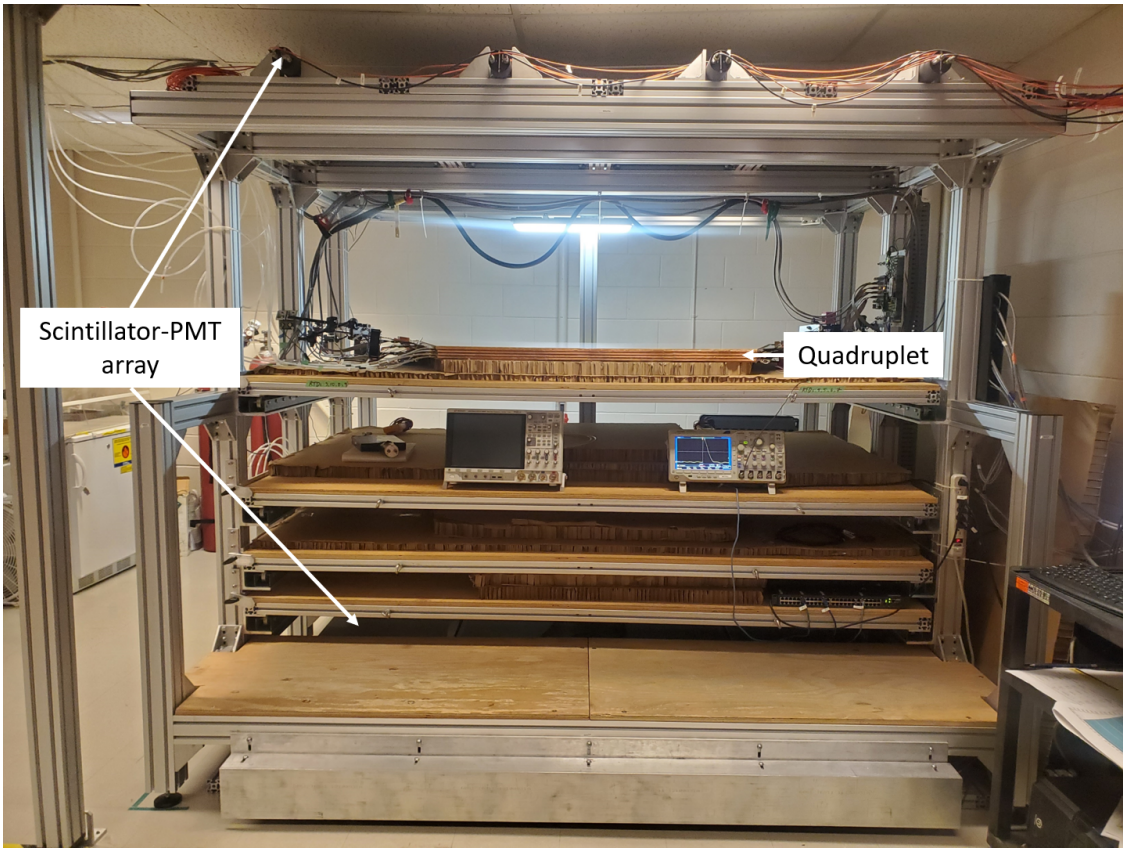


Figure 4.1: Cosmic muon hodoscope at McGill University with sTGC quadruplet in the test bench.

615 4.2 Experimental setup

616 Cosmic muon characterization was done with a hodoscope, a complete description of which
 617 can be found in [59]. The quadruplet was placed in the center of the test bench. Above
 618 and below it was a layer of scintillator-PMT arrays, labeled in figure 4.1. When a cosmic
 619 muon passed within the acceptance of the hodoscope, at least one scintillator from the top
 620 array and at least one from the bottom array fired in coincidence. The coincident signal was
 621 used to trigger the readout of the quadruplet's electrodes using NIM modules. The trigger
 622 was passed to the front-end electronics attached to the adaptor boards of each layer of the
 623 quadruplet.

624 Operating the chambers also required gas and high voltage. A pentane-CO₂ mixture was
 625 mixed and delivered to each sTGC with a gas system designed and made at McGill University.

626 The gas system was controlled by a slow control program, also made in-laboratory [60].
627 Although gas mixture is flammable, it allows the chambers to operate in high amplification
628 mode without production of excess photons saturating the signal across many strips because
629 pentane absorbs a wide energy of photons [55]. To prepare the quadruplets for operation,
630 CO_2 was flushed through them overnight to remove impurities. Then, five gas volumes of
631 the pentane- CO_2 mixture was flushed through (approximately 3 hours). High voltage was
632 provided by CAEN boards.

633 4.3 Data acquisition

634 Each sTGC electrode was connected to a channel on a prototype ASIC¹ on the front-end
635 electronics, attached to the adaptor boards on each layer of a quadruplet. The ASIC ampli-
636 fied the signal and was set to measure and record the signal peak amplitude from electrodes.
637 For each trigger, the signal peak amplitude of all channels above threshold was recorded
638 as an event and stored in a binary file. Channel thresholds were estimated [62] and ad-
639 justed manually in the configuration/readout software before the start of data acquisition.
640 There was an exception to the threshold rule: the signals on strips adjacent to a strip above
641 threshold were also readout using the so-called “neighbour triggering” function of the ASIC.
642 The quadruplets were held at 3.1 kV for approximately two hours to collect data from 1
643 million muon triggers.

644 4.4 Data preparation

645 4.4.1 Cuts on electrode hits

646 Corrupted data is removed while the raw data is being recorded in a binary file. The binary
647 file is decoded into a usable ROOT [63] tree offline.
648 A hit is defined as a signal recorded from a channel that was above threshold or (in the
649 case of strips) neighbour triggered. In addition to hits from muons, the quadruplets record
650 noise from the electronics and δ -rays (electrons liberated with sufficient energy to cause more
651 ionization before acceleration). Therefore, cuts are applied to reduce the number of noise
652 hits. The edge strips are very noisy, so all strip hits on layers with strip hits on either
653 edge channel are cut. A default pedestal value is subtracted from the recorded signal peak

¹the VMM3 [61], designed for the MMs and sTGCs of the NSW

654 amplitude of each electrode for a more realistic estimate of the signal amplitude. Also, events
655 that only have hits on pad electrodes (no strips or wires) were cut because the large area of
656 the pads made them susceptible to noise.

657 4.4.2 Clustering and tracking

658 Many of the high-level characterization metrics require rebuilding muon tracks. For events
659 passing quality cuts, the x - and y -coordinates of the ionization avalanche on each layer are
660 extracted from the signal on the wires and strips respectively for each event, as is sketched in
661 figure 4.2. In this work, x is the coordinate perpendicular to the wires and y is the coordinate
662 perpendicular to the strips.

663 The x -coordinate is taken as the center of the wire group with the maximum peak signal
664 amplitude, since the wire groups' pitch (36 mm) is larger than the typical charge spreading.
665 Assuming that the true x -position of the hit is sampled from a uniform distribution over the
666 width of the wire group, the uncertainty in the x -position was given by $\frac{36}{\sqrt{12}}$ mm = 10 mm [64].

667 The y -coordinate is taken as the Gaussian mean of the peak signal amplitude distribution
668 across groups of contiguous strips. The process of grouping contiguous strip hits on a layer is
669 called clustering, and the resulting group is called a cluster. Figure 4.2 sketches the clustering
670 process and a sample cluster is shown in figure 4.3. The data acquisition system recorded
671 the electrode ID of the strip hit and in the clustering process the position of the center
672 of the strip electrode is calculated based on the nominal quadruplet geometry. Typically,
673 clusters are built of 3-5 strips. The thickness of the graphite coating over the cathode boards
674 determined how many strips picked up the ionization image charge. Larger clusters were
675 more likely caused by δ -rays since they spread the cloud of ionization.

676 Events are cut from the analysis if there are two clusters on one layer's set of strips (indicative
677 of noise). Clusters are cut if the cluster size is lesser than three (which should not happen for
678 real events thanks to neighbour triggering), and if the cluster size is greater than 25. After
679 all the cuts on hits and clusters, roughly half as many muon tracks as triggers collected
680 remain.

681 The uncertainty in the y -coordinate could have been taken as the fitted cluster mean's
682 statistical uncertainty; however, after comparing the difference in cluster means for different
683 fitting algorithms in appendix A.2, 60 μm of uncertainty was assigned.

684 The coordinates of the avalanches' on all layers were used to reconstruct tracks in x and y
685 respectively. The tracks were then used to calculate characterization metrics like electrode
686 efficiency and spatial resolution, the details of which are discussed in [59].

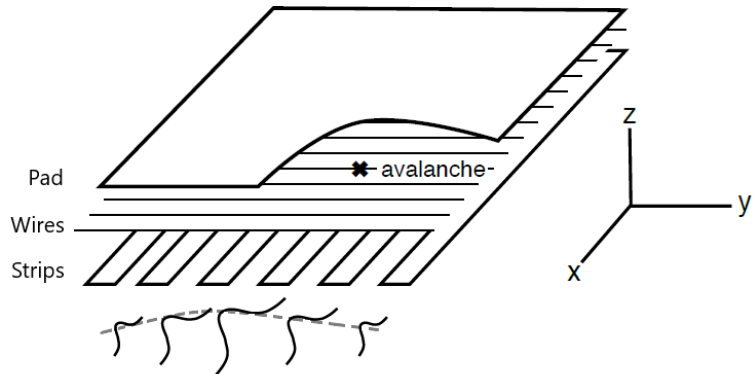


Figure 4.2: A sketch of an sTGC-like detector. The position of the avalanche is extracted from the wires and strips that picked up the avalanche signal. The signals on individual strips are sketched. Clustering was the processs of fitting a Gaussian to the peak value of the signals on individual contiguous strips, as is done in figure 4.3. In this work, the $x(y)$ -coordinate will always refer to the coordinate perpendicular to the wires (strips) [59, 56].

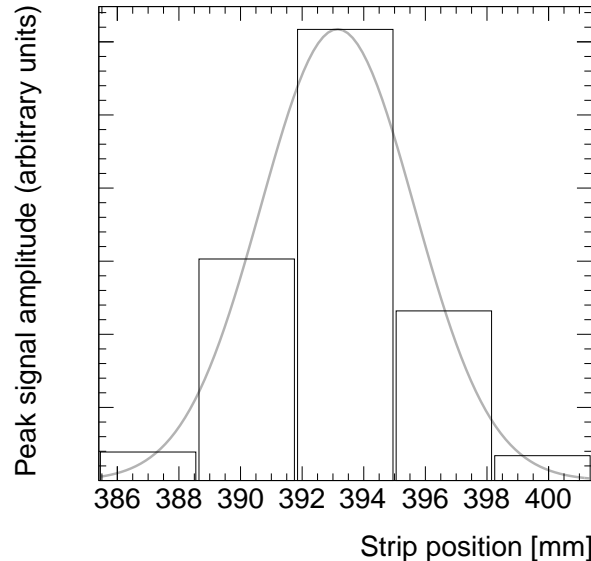


Figure 4.3: A sample cluster resulting from the current picked up on a group of strips after the passing of a muon (presumably). The grey curve is a Gaussian fit.

687 4.5 Measuring relative local offsets

688 The offset of a strip from its nominal position can be modeled as a passive transformation.
689 For each area of a strip layer, the local offset is the shift of the strip pattern in that area with
690 respect to the nominal geometry. Local offsets systematically change the set of strips nearest
691 to muons passing through the area. The data preparation software assumes that strips are
692 in their nominal positions, so the recorded muon y -position on layer i , y_i , is shifted opposite
693 to the layer's local offset, $d_{local,i}$, by

$$y_i = y_{nom,i} - d_{local,i}, \quad (4.1)$$

694 where $y_{nom,i}$ is the position of the muon that would have been recorded on layer i if there
695 was no local offset. Equation 4.1 ignores other factors that affect the cluster position, like
696 position resolution. With cosmics data, the local offset is unknown and there was no external
697 reference to measure $y_{nom,i}$. Therefore, only relative local offsets could be calculated.

698 The minimal relative coordinate system uses two reference or fixed layers [59]. The hits
699 on the two fixed layers were used to create tracks that can be interpolated or extrapolated
700 (polated) to the other two layers. The set of two fixed layers and the layer polated to are
701 referred to as a tracking combination. The residual of track i , Δ_i is defined as,

$$\Delta_i = y_i - y_{track,i}, \quad (4.2)$$

702 where $y_{track,i}$ is the polated track position. Track residuals are affected by the relative local
703 offset in the area of each layer's hit. As an example, in figure 4.4, the residual on layer
704 2 perhaps indicates that layer 2 is offset with respect to layers 1 and 4 in the area of the
705 track. Of course, a single track residual says nothing of the real relative local offset because
706 of the limited spatial resolution of the detectors and fake tracks caused by noise or delta
707 rays. However, the mean of residuals for all tracks in a region will be shifted systematically
708 by the local offsets between layers [59]. For a quadruplet with nominal geometry, the mean
709 of residuals should be zero in all regions and for all reference frames, unlike the example
710 regions in figure 4.5. The value of the mean of residuals is a measure of the relative local
711 offset of the layer with respect to the two fixed layers.

712 To study the relative local offsets, residual distributions across each strip layer of a quadruplet
713 for all tracking combinations were assembled and fitted. The residual distributions were
714 wider for tracking combinations where the extrapolation lever arm was largest, as in the
715 example distributions shown in figure 4.5. In general, residual means from distributions of
716 residuals with geometrically less favourable tracking combinations have larger statistical and
717 systematic uncertainties. The bin size of 200 μm for the distributions shown in figure 4.5 was

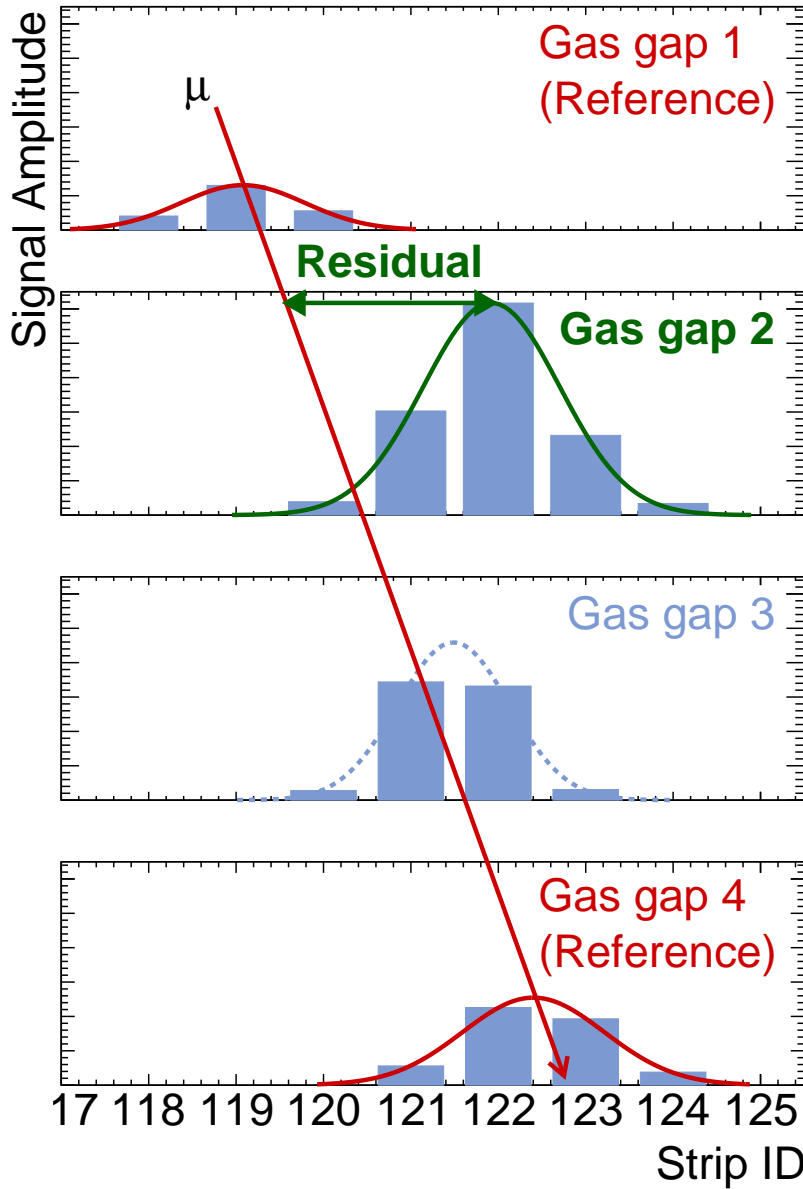
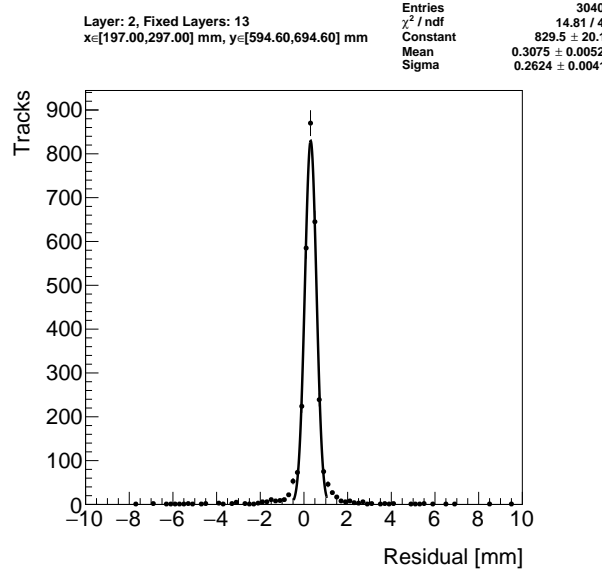
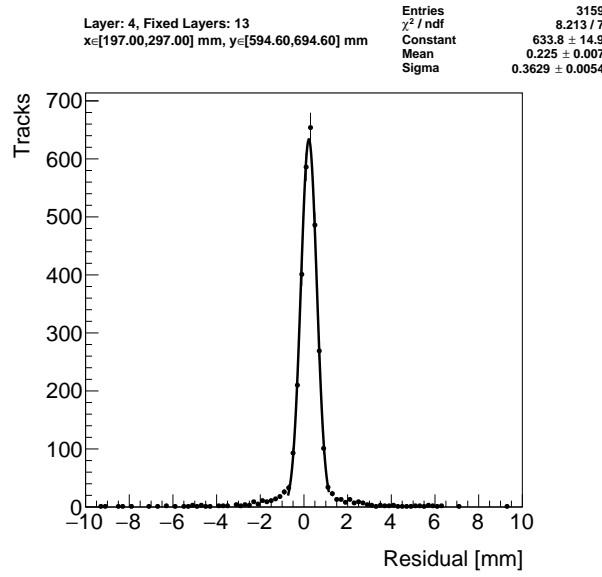


Figure 4.4: Representation of a muon event recorded by an sTGC. The clusters are fit with a Gaussian and the mean is taken as the hit position. A track is built from the chosen reference layers, 1 and 4, and the residual calculated on layer 2. The clusters come from a real muon, but their positions were modified to highlight the residual on layer 2.



(a) Tracks on layer 2, reference layers 1 and 3.



(b) Tracks on layer 4, reference layers 1 and 3.

Figure 4.5: Residual distribution in the region $x \in [197, 297]$, $y \in [594.6, 694.6]$ mm (100 mm by 100 mm area) for two different tracking combinations. Data from quadruplet QL2.P.11.

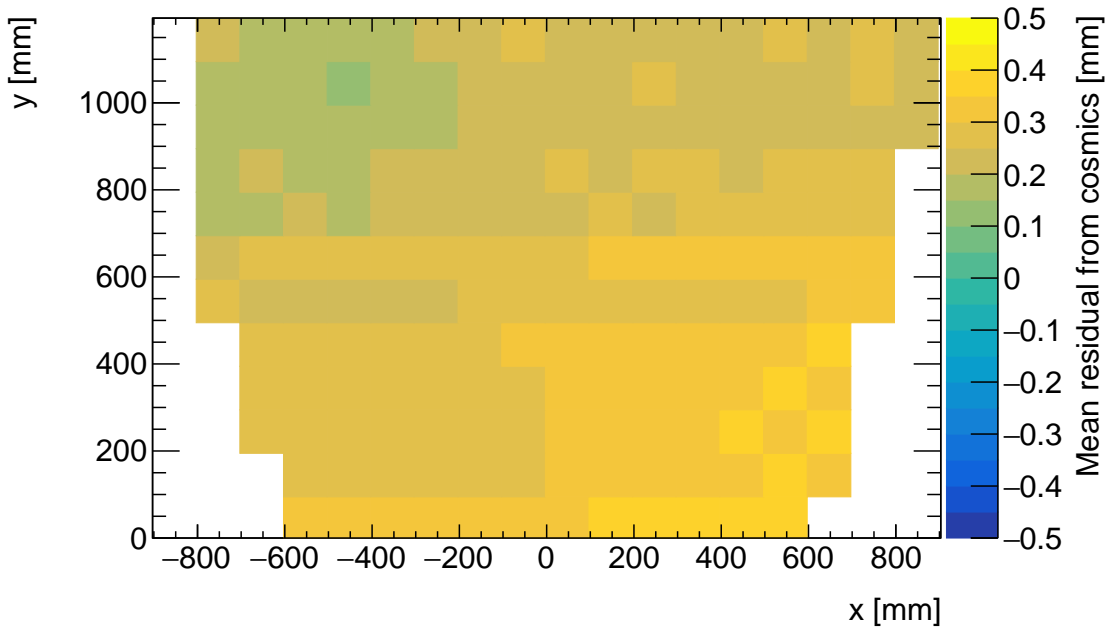
718 chosen based on the uncertainty on residuals calculated from tracks on layer 4 (1) built from
719 hits on layers 1 and 2 (3 and 4) given a cluster y -position uncertainty of $60 \mu\text{m}$ (appendix A.3),
720 since these tracks yield residuals with the largest uncertainties.

721 A gaussian fit was used to extract the mean of the residual distributions. Theoretically, a
722 double gaussian distribution is more apt, but for this analysis the gaussian fit was sufficient,
723 as discussed in appendix C.1.

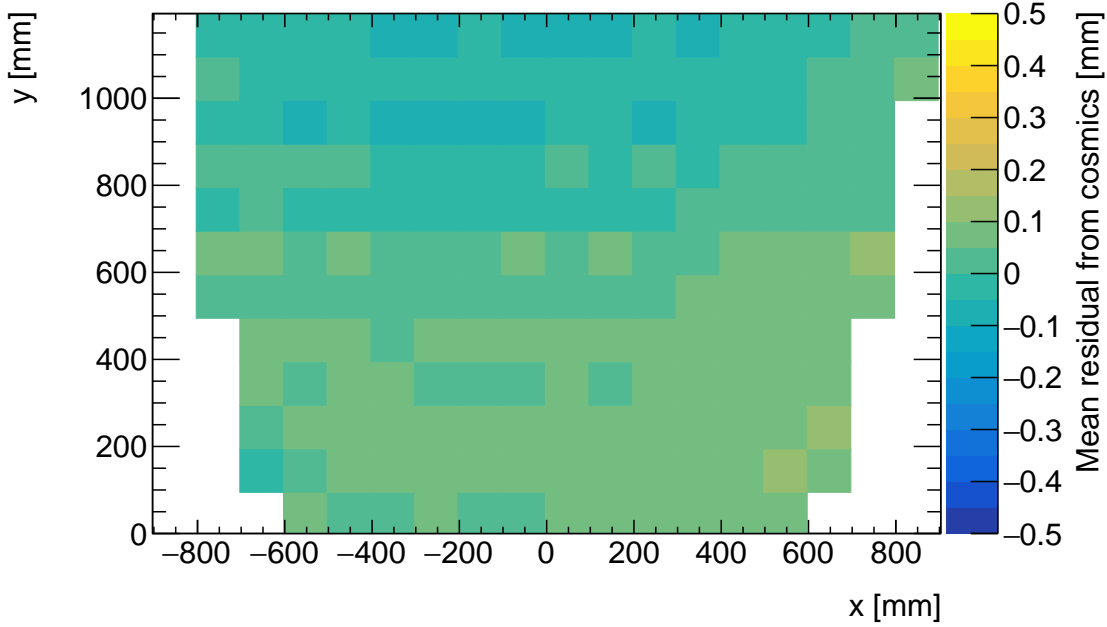
724 The area of the region of interest was 100 mm by 100 mm. The size balanced the amount of
725 tracks falling in the region of interest to give a small statistical uncertainty on the extracted
726 mean while being smaller than the order on which local offsets were expected to change
727 significantly. The change in local offsets over the surface of a layer can be modeled using
728 global alignment parameters. Using a base alignment model with a global offset and rotation
729 of each strip layer, “significantly” was defined by the distance in x that a large but possible
730 rotation of $1000 \mu\text{rad}$ would change the local offset by more than $50 \mu\text{m}$ – half the required
731 position resolution of the sTGCs [5].

732 4.6 Visualizing relative alignment between layers

733 The mean of residuals was plotted across entire strip layers for every tracking combination to
734 get a picture of the how relative local offsets change over the layers’ surface. Figure 4.6 shows
735 the mean of residuals on layer 2 with reference layers 1 and 3 for two different quadruplets,
736 referred to as QL2.P.11 and QL2.P.8, for 100 mm by 100 mm areas across the surface of
737 layer 2. To understand these plots, realize that the Gaussian mean of the distribution in
738 figure 4.5a is the entry in area bin $x \in [197, 297]$, $y \in [594.6, 694.6]$ mm in figure 4.6a.



(a) Mean of residuals of tracks on layer 2, reference layers 1 and 3, for QL2.P.11.



(b) Mean of residuals of tracks on layer 2, reference layers 1 and 3, for QL2.P.8.

Figure 4.6: Mean of residuals in each 100 mm by 100 mm bin over the area of the layer 2 cathode board. The entry in $x \in [197, 297]$, $y \in [594.6, 694.6]$ mm of figure 4.6a corresponds to the fitted Gaussian means in figures 4.5a. The mean of residuals is an estimate of the local offset of layer 2 with respect to layers 1 and 3.

Many of the residual means are non-zero and change smoothly over the layer, indicating that there are relative local offsets stemming from misalignments between entire strip layers. Given that the residual mean changes with x in figure 4.6a, there is likely a rotation of layer 2 with respect to layers 1 and 3 on QL2.P.11, combined with an offset of the entire layer. The residual means are smaller in figure 4.6b indicating that QL2.P.8 is less misaligned overall than QL2.P.11; however the relative local offsets range between $\pm 200 \mu\text{m}$ so they are still significant considering the order on which the chambers must be sensitive to position, $\sim 100 \mu\text{m}$.

4.7 Systematic uncertainty

The statistical uncertainty on the local residual means was typically around $10 - 20 \mu\text{m}$, and appendix B shows that the analysis was not statistically limited by the number of triggers collected for each quadruplet. The systematic uncertainties were more significant.

Systematic uncertainties were assigned per tracking combination as the RMS of the distribution of the difference in local residual means each calculated in a different way. For example, the RMS associated with fitting the local residual distributions with a Gaussian or double Gaussian is $25 \mu\text{m}$ for the geometrically least favourable tracking combinations. The distribution is shown in appendix C.1. For geometrically similar tracking combinations (like: tracks on layer 1 built from hits on layers 3 and 4, and tracks on layer 4 built from hits on layers 1 and 2), the systematic uncertainty was assigned as the average RMS of both.

Other choices were: whether to use data collected at 2.9 kV or 3.1 kV (both are collected at McGill); what cluster fitting algorithm to use; and whether or not to apply a differential non-linearity (DNL) correction to the cluster y -positions. A systematic uncertainty was assigned using the method above to account for the effect of each choice and quantify the robustness of the mean of residuals. The reasons for each choice are listed below.

Data taken at 3.1 kV was used over 2.9 kV because the strip and wire tracking efficiency increases with higher voltage [59] (appendix C.2).

The Minuit2 package [65] was used to fit clusters over Guo's method [66] because it provided automatic statistical uncertainty estimates and is the standard fit algorithm of ROOT [63] (appendix C.3).

The DNL correction was not applied because its effect on the residual means was negligible (appendix C.4).

A summary of the systematic uncertainties assigned for each tracking combination is given in table 4.1.

Tracking geometry	Residual distribution fit function (C.1)	Cosmics data collection voltage (C.2)	Cluster fit algorithm (C.3)	Apply DNL correction or not (C.4)	Total
Similar to layer 3, fixed layers 1, 2	0.01	0.04	0.02	0.01	0.05
Similar to layer 4, fixed layers 1, 2	0.03	0.01	0.03	0.01	0.10
Similar to layer 2, fixed layers 1, 3	0.01	0.02	0.01	0.000	0.03
Similar to layer 4, fixed layers 1, 3	0.01	0.04	0.01	0.01	0.04
Similar to layer 2, fixed layers 1, 4	0.01	0.04	0.01	0.01	0.04

Table 4.1: Systematic uncertainty assigned for each analysis option, detailed in appendix [C](#).

772 The uncertainty in each mean of residuals was assigned as the sum in quadrature of the sta-
773 tistical uncertainty in the mean and the appropriate systematic uncertainty for the tracking
774 combination.

775 4.8 Discussion

776 Cosmics data is being used to calculate relative alignment parameters using two other meth-
777 ods [59]. A cross-check of this analysis would be to compare their results; however the studies
778 in appendix C show that the mean cosmics residuals are robust, so the comparison was not
779 prioritized.

780 Given that the uncertainty in the residual means is lesser than or near to the order of the
781 required position resolution of the sTGCs (100 μm [5]) they are relevant input for alignment
782 studies.

783 The relative local offsets as calculated from the mean of residual distributions provide a
784 complete picture of the relative alignment between detectors planes. In fact, cosmic muon
785 testing is the only characterization technique where the entire surface of quadruplet layers
786 can be probed since muons hits are distributed almost uniformly; the CMM [7] and x-ray
787 methods [8] depend on measurements at reference points, and test beams only have a limited
788 beam spot [6]. By looking at 2D-histograms of residual means like figure 4.6 for all tracking
789 combinations, it is easy to identify quadruplets that suffer large relative misalignment since
790 many residual means differ significantly from zero. Moreover, the pattern in the relative
791 local offsets can be used to motivate a physical interpretation of misalignments. The relative
792 local offsets can be used as a reference, cross check, or input in other alignment studies.

793 Relative local offsets cannot be used to position strips in the absolute ATLAS coordinate
794 system because there was no external reference to measure positions on all layers with re-
795 spect to. The lack of external reference means that there is not enough information to unfold
796 relative local offsets into absolute local offsets (with respect to the nominal quadruplet ge-
797 ometry). As an example, assuming that the residual on layer 2 in figure 4.4 is representative
798 of the relative local offset, the residual on layer 2 could be caused by the strips on layer 2
799 being misaligned from nominal, but it could also be caused by strips on layers 1 and 4 being
800 offset from nominal while the strips on layer 2 are in their nominal positions! Any number
801 of combinations of local offsets on layers 1, 2 and 4 could produce the residual on layer 2.
802 Absolute local offsets must be calculated another way.

803 **Chapter 5**

804 **Using x-rays to measure relative strip
805 position offsets**

806 Local offset measurements were done with the x-ray method. The reader is referred to the
807 paper describing the x-ray method [8], although some minor changes have been made to the
808 experimental setup since it was written. The experimental setup described here is current
809 and was used to collect the data presented in this thesis.

810 **5.1 Experimental setup**

811 The x-ray tests were performed after the quadruplets arrived at CERN, were assembled into
812 wedges, and alignment platforms installed. Essentially, an x-ray gun was attached to one
813 of the alignment platforms glued to the surface of the wedge and the x-ray beam profile
814 recorded by the strips.

815 The wedges were installed on carts that could rotate their surface to a horizontal position. A
816 mounting platform was installed on top of the alignment platform using a three-ball mount.
817 The x-ray gun used was an [Amptek Mini-X tube](#). The gun was placed in a brass holder
818 with built-in 2 mm collimator and 280 μm copper filter. The holder was mounted on one
819 of five positions on the mounting platform, as shown in figure 5.1. Gun positions were
820 chosen to avoid wire support structures in the sTGCs that reduce hit efficiency [59] and
821 boundaries between sets of strips read out by two different ASICs that could each have
822 different thresholds.

823 As with cosmics data collection, each sTGC also needed gas and high voltage to operate.

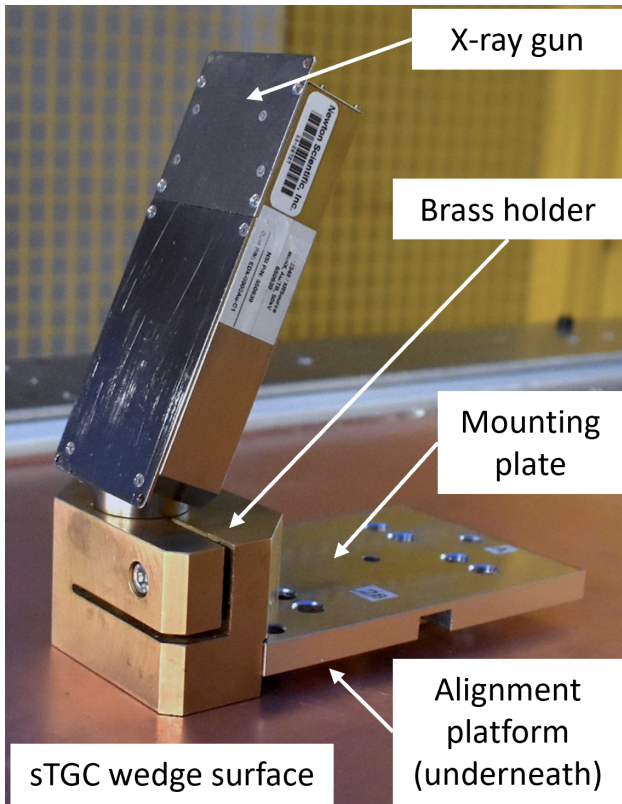


Figure 5.1: The x-ray gun mounted to the alignment platform on the surface of the wedge.
Adapted from [8].

824 Each layer was operated at 2.925 kV with high voltage from a NIM crate. The chambers
825 were flushed with CO₂ before and during data collection.
826 The gun produced x-rays with energies under 40 keV with peaks in the 7-15 keV range. The
827 x-rays mostly interacted with the wedge's copper electrodes and gold-plated tungsten wires
828 via the photo effect. The resulting photoelectrons caused ionization avalanches that were
829 picked up by the strips.

830 5.2 Data acquisition

831 A different version of the same front end electronics, but the same ASIC, as used in cosmics
832 testing were used for the x-ray testing to amplify the data and measure the peak signal
833 amplitude. Data was collected for two minutes per gun position with random triggers. A
834 trigger recorded all signals above threshold. Pad and wire data was not recorded.

835 5.3 Data preparation

836 Like with cosmics analysis, a default pedestal is subtracted from the signal peak amplitude
837 on each electrode.
838 Clusters are defined as groups of contiguous strip hits collected within 75 ns. The peak signal
839 amplitude of each electrode in a cluster is fit with a Gaussian, and the mean of the Gaussian
840 is taken as the cluster position. Cluster positions are corrected for DNL (see definition in
841 appendix C.4). Only clusters composed of hits on 3-5 strips were used in the x-ray analysis.
842 Clusters with signal on more than 5 strips were cut because they were most likely caused by
843 photoelectrons ejected with enough energy to be δ -rays.
844 The x-ray analysis diverges entirely from the cosmics analysis algorithm here because the
845 x-rays do not leave tracks. The signals picked up by the strips are from photoelectrons
846 liberated from the metals of the sTGCs, which only travel through one gas volume and are
847 ejected at all angles. Instead of creating tracks, the cluster position distribution on each
848 layer is used to define the beam profile. A typical beam profile is shown in figure 5.2.

849 5.4 Measuring local offsets

850 The mean of the cluster position distribution is taken as the x-ray beam profile center.
851 The expected center is calculated assuming a wedge with nominal geometry given the gun



Figure 5.2: Distribution of x-ray cluster mean positions after the analysis cuts and corrections. The strip cluster multiplicity, m , was limited to 3, 4 and 5. The red curve is a Gaussian fit of the distribution and the pink dashed lines denote the edges of the strips [8].

position, corrected for: the geometry of the brass holder, the positioning and angle of the alignment platforms and the beam angle. The difference between the expected and reconstructed beam profile center is a measure of the local offset. Applying the logic of equation 4.1 to the beam profile, the Gaussian mean of cluster positions on the given layer acts as the recorded position, y_i , the expected center is $y_{nom,i}$ and the local offset is $d_{local,i}$ as before, where i denotes the layer. Since the position of the alignment platforms will be monitored by the alignment system in ATLAS [5], the position of the strips that should have been at the gun position are shifted by $d_{local,i}$ and so are known in the ATLAS coordinate system for every position where x-ray data was taken.

The x-ray working group accepted an uncertainty of 120 μm on the beam profile centers. The largest uncertainty comes from the effect of the gun angle, which proved difficult to measure and correct for.

The local offsets are not presented here as the author did not conduct this work. However, the author used the local offsets to calculate relative local offsets.

5.5 Measuring relative local offsets

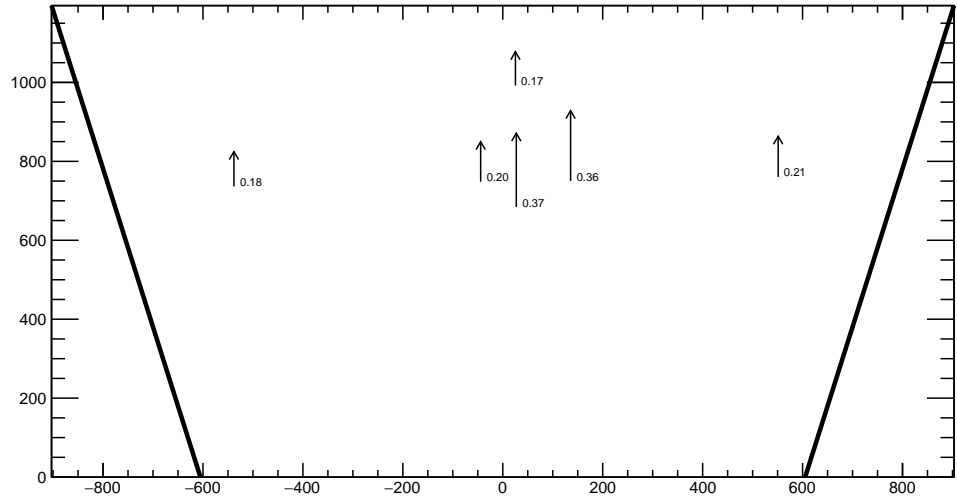
The x-ray local offsets were shown to be correlated with the local offsets calculated from the CMM data, but the CMM data does not include the effect of inter-layer misalignments so the degree of correlation measurable was limited. Cosmics data is affected by inter-layer misalignments. Since the local offsets for x-rays and cosmics data are measured in different coordinate systems, they cannot be compared directly. Bringing the cosmics relative local offsets into an absolute coordinate system is impossible; however, the x-ray local offsets can be brought into a relative coordinate system.

The measured x-ray beam profile centers were systematically affected by local offsets in the same way as the mean cosmics residuals, as modeled by equation 4.1. Therefore, if a 2-layer track is built from the beam profile centers on each layer and the residual calculated on a third layer, that residual should match the local mean cosmics residual. The residual is the difference between the beam profile center on the layer of interest and the polated track position from the beam profile centers recorded on the two fixed layers. The beam profile center on the layer of interest acts as y_i and the polated track position acts as $y_{track,i}$ in equation 4.2.

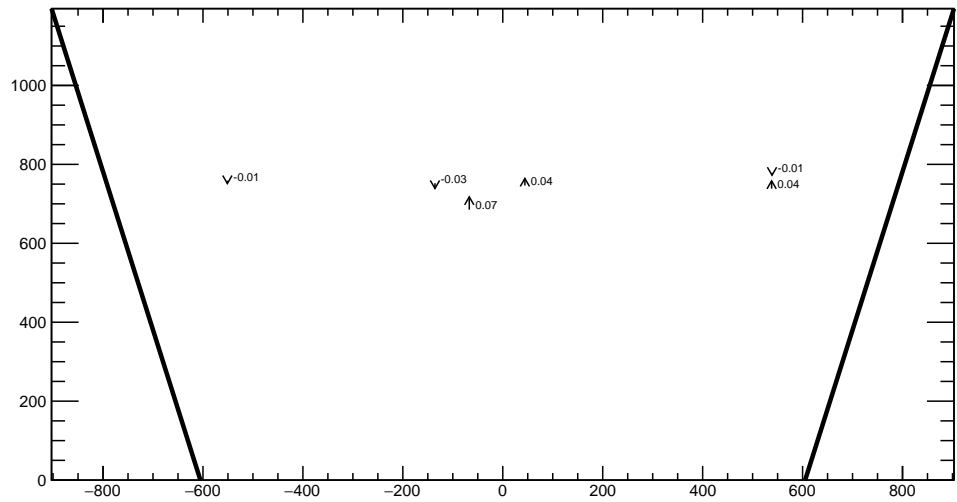
The built track is not an actual track of the x-ray beam. A beam profile center is actually the Gaussian mean of all selected mean cluster positions recorded during the x-ray data taking period, not a single hit of a track. Building an “abstract” track was necessary because

885 the x-rays cause signal in the chamber via the photoeffect so there were not individual “x-
886 ray tracks” to record. In fact the x-ray data could be collected separately for each layer.
887 Nonetheless, since the effect of local offsets on the beam profile centers was the same as their
888 effect on the recorded cosmics cluster positions the difference in algorithm between x-ray
889 and cosmics analysis was allowed.

890 For each x-ray survey position, the x-ray residual was calculated for all possible tracking
891 combinations (which required an x-ray beam profile on at least three layers). The x-ray
892 residuals on layer 2 calculated from the beam profile centers recorded on layers 1 and 3 are
893 represented as arrows in figure 5.3 as arrows for QL2.P.11 and QL2.P.8. For QL2.P.11, a
894 negative offset at all x-ray survey positions is clear.



(a) QL2.P.11 x-ray residuals on layer 2, reference layers 1 and 3.



(b) QL2.P.8 x-ray residuals on layer 2, reference layers 1 and 3.

Figure 5.3: The x-ray residuals on layer 2 calculated from the beam profile centers recorded on layers 1 and 3 for QL2.P.11 and QL2.P.8. The arrows originate from the expected position of the beam profile center assuming a nominal geometry, and the lengths are proportional to the calculated x-ray residuals. The tip of the arrow represents where the recorded hit was with respect to where it should have been recorded nominally. The value of the x-ray residuals are annotated in millimeters and have an uncertainty of ± 0.15 mm.

895 The uncertainty on the x-ray residuals was the error propagated through the tracking, taking
896 an uncertainty of 120 μm on each beam profile center. The uncertainty on the x-ray residuals
897 ranged from 0.15 mm to 0.4 mm from the most to least geometrically-favourable tracking
898 combination. There is no discernible pattern to the x-ray residuals on QL2.P.8 because they
899 are smaller than the uncertainty. The x-ray residual uncertainties are significantly larger
900 than the uncertainties on the relative local offsets calculated with cosmics data.

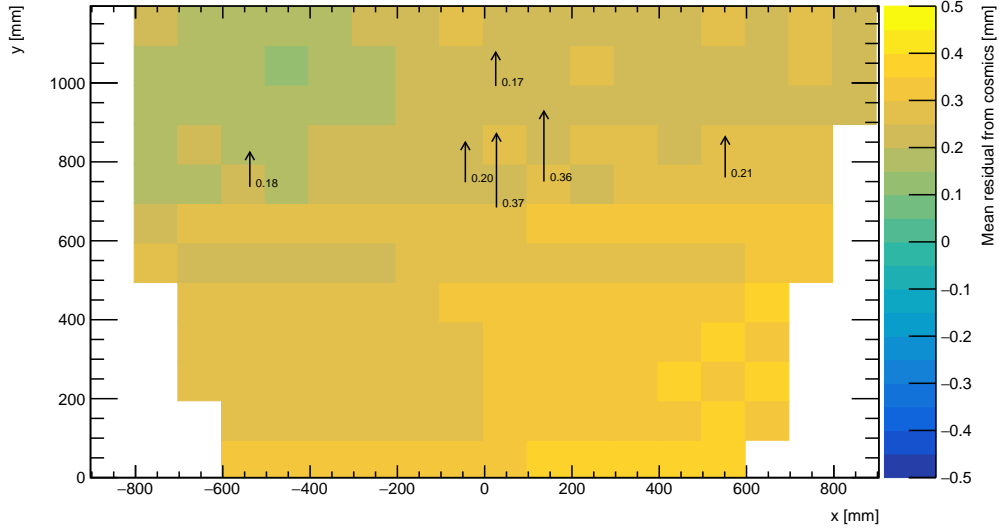
901 **Chapter 6**

902 **Comparing cosmic muon and x-ray
903 relative strip position offsets**

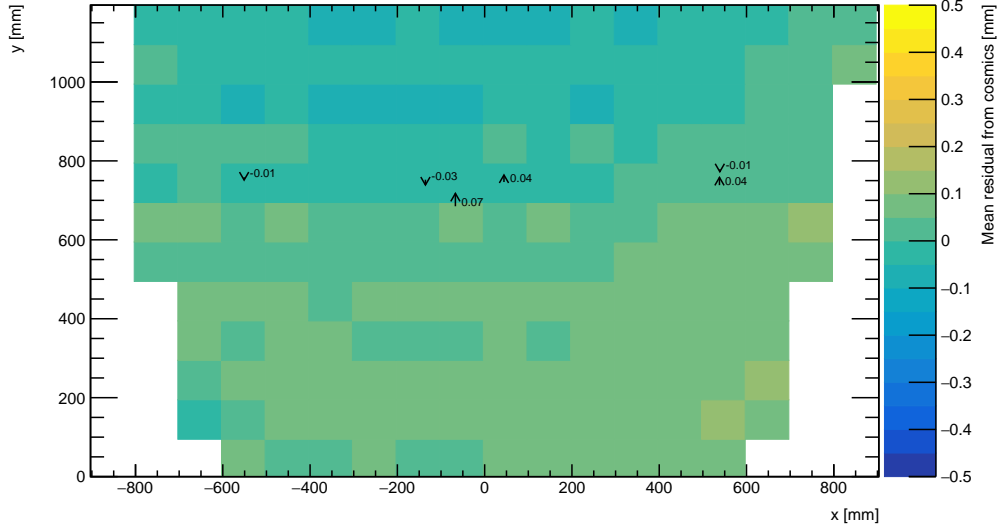
904 The goal was to validate the local offsets extracted from the x-ray data with cosmics data.
905 The complication was that the x-ray dataset provided absolute local offsets while the cosmics
906 dataset provided relative local offsets, which could not be compared directly. The solution
907 was to use the x-ray local offsets to calculate relative local offsets. The x-ray relative local
908 offset is the x-ray residual reconstructed from an abstract track using the beam profile
909 centers on each layer as the track hits. The cosmics relative local offset was taken as the
910 Gaussian mean of muon track residuals in a 100 mm by 100 mm area, referred to as the
911 the mean cosmics residual. Relative local offsets of each type calculated using the same
912 reference layers are compared for each area where x-ray data is available. The results of the
913 comparison are presented here.

914 **6.1 Assessing correlation**

915 The 2D visualizations of the mean cosmics and x-ray residuals for tracks on layer 2 with
916 reference layers 1 and 3 on QL2.P.11 and QL2.P.8 are shown in figure 6.1. Figure 6.1 is a
917 superposition of figures 4.6 and 5.3.



(a) QL2.P.11 residuals of tracks on layer 2, reference layers 1 and 3.



(b) QL2.P.8 residuals of tracks on layer 2, reference layers 1 and 3.

Figure 6.1: The mean cosmics residuals are shown using colour. The x-ray residuals available at nominal gun positions are drawn as arrows and the value of the residual annotated in millimeters with uncertainty ± 0.15 mm. The length of the arrows is 500 times the value of the x-ray residual, scaled for visibility. These plots are a superposition of figures 4.6 and 5.3.

918 Figure 6.1a shows that for QL2.P.11 the x-ray residuals are of the same sign and order as
919 the mean cosmics residuals, as can be seen by comparing the the annotated value of the
920 x-ray residual to the mean cosmics residual represented by colour; QL2.P.11's mean cosmics
921 and x-ray residuals are correlated to some degree. For QL2.P.8, the x-ray residuals are of
922 the right order compared to the mean cosmics residuals, but the correlation is less apparent.
923 While x-ray residuals do not reveal a pattern across the layer's surface, the mean cosmics
924 residuals show a structure to the relative local offsets since they vary smoothly over the
925 surface of layer 2.

926 The comparison of mean cosmics and x-ray residuals was done for several quadruplets for
927 all tracking combinations (not just layer 2 residuals calculated with fixed layers 1 and 3 like
928 in figure 6.1). Scatter plots of the x-ray and mean cosmics residuals on QL2.P.11 and -2
929 for all tracking combinations shown in figures 6.2 and 6.3 reveal the degree of correlation
930 between the datasets. In the correlation plots, each rectangle is centered on the value of a
931 mean cosmics and x-ray residual pair calculated with a given tracking combination for every
932 gun position where data is available; the height and width of the squares are the uncertainty
933 in the mean cosmics and x-ray residuals respectively. Note that in the scatter plots, the
934 regions of interest where cosmics tracks are included in the calculation of mean of residuals
935 are exactly centered on the nominal x-ray beam position, unlike in figure 6.1.

936 The fitted slope and offset in figure 6.2 show that the two QL2.P.11 datasets are correlated.
937 The large uncertainty on the x-ray residuals set a limit on the sensitivity of the analysis,
938 for if the absolute value of the x-ray residuals of a quadruplet were smaller than the x-ray
939 residual uncertainties, no conclusion about the correlation could be drawn, like for QL2.P.8
940 (figure 6.3). This result is reflected in the small x-ray residuals shown in figure 6.1b that
941 do not reveal a pattern in the relative local offsets across the surface of layer 2. However,
942 figure 6.3 shows that the x-ray and mean cosmics residuals are centered around zero, as is
943 expected for a quadruplet with small relative misalignments between layers.

944 There are three patterns in the residuals on the scatter plot explained by geometry. First,
945 for both datasets the uncertainty in the extrapolated track residuals were larger than the
946 interpolated track residuals because of the extrapolation lever arm. For the x-ray residuals,
947 the effect of the lever arm on the uncertainty was direct since the residual was calculated from
948 a single abstract track; for the mean cosmics residuals it was the widening of the residual
949 distribution due to the extrapolation lever arm that increased the uncertainty in the fitted
950 mean of residuals. Second, residuals calculated through extrapolation tend to be larger
951 because the extrapolation lever arm can produce more extreme values of the track position
952 on the layer of interest. Third, the points in figure 6.2 are geometrically correlated (e.g.
953 they seem to be roughly mirrored around the origin). This is expected since the residuals
954 calculated using a given set of three layers should be geometrically correlated by the local

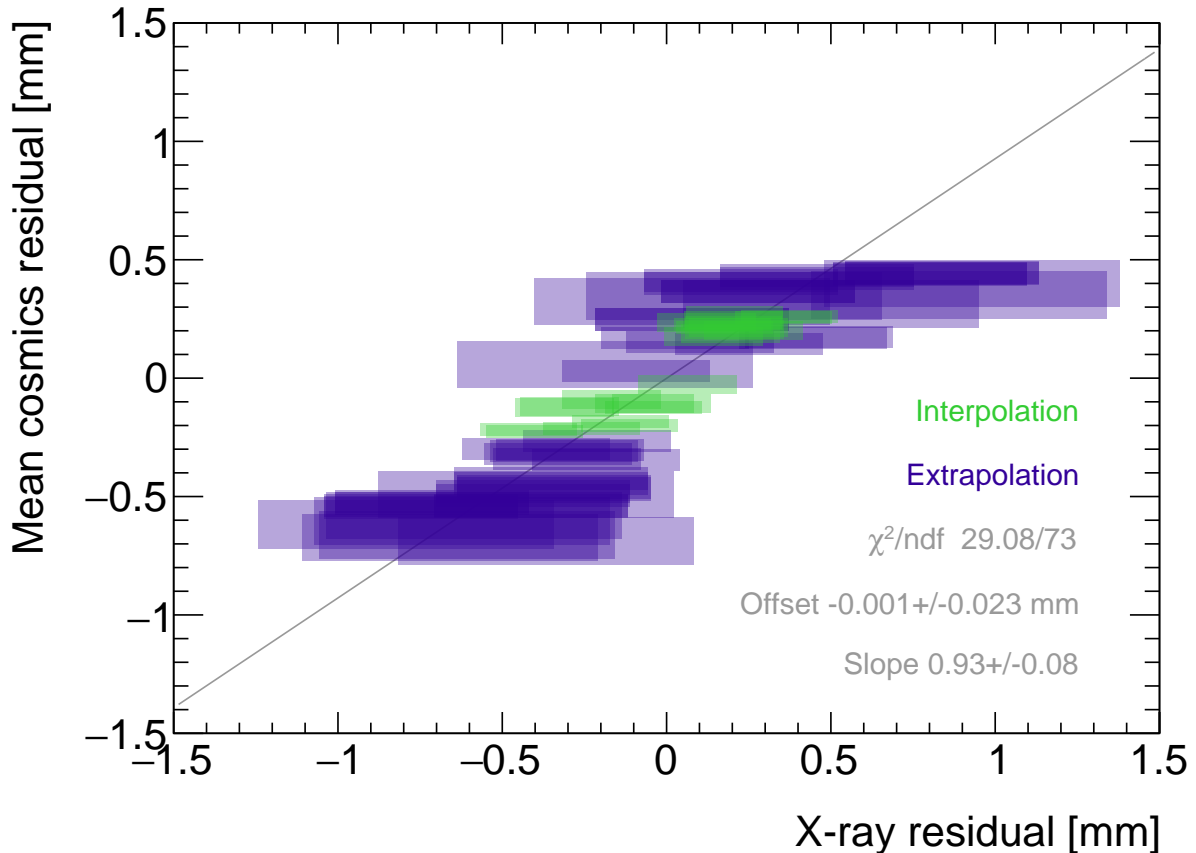


Figure 6.2: Correlation plot between x-ray and mean cosmics residuals for all tracking combinations for QL2.P.11. Each rectangle is centered on an x-ray and mean cosmics residual pair calculated at a given gun position and for a certain tracking combination. The width of the rectangles in x and y are the uncertainty in the x-ray and mean cosmics residual respectively. A printer-friendly version of this plot is available in appendix D.

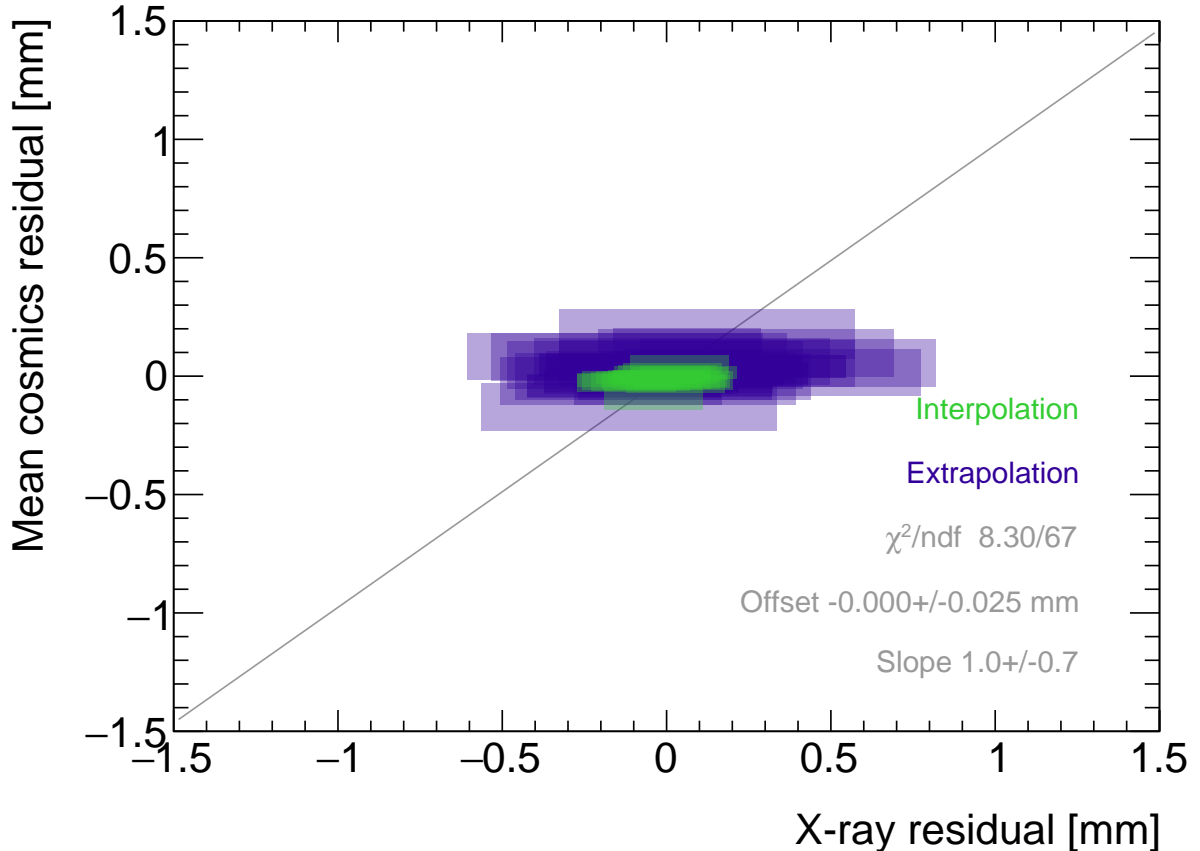


Figure 6.3: Correlation plot between x-ray and mean cosmics residuals for all tracking combinations for quadruplet 2. Each rectangle is centered on an x-ray and mean cosmics residual pair calculated at a given gun position and for a certain tracking combination. The width of the rectangles in x and y are the uncertainty in the x-ray and mean cosmics residual respectively. A printer-friendly version of this plot is available in appendix D.

955 offsets on the fixed layers and the layer of interest (the $d_{local,i}$ on each layer as defined in
956 equation 4.1).

957 6.2 Discussion

958 Several quadruplets were tested for each quadruplet construction geometry built in Canada.
959 Each quadruplet fell into one of the two categories: residuals large enough to see a correlation,
960 or residuals too small to see a correlation. Since the x-ray and mean cosmics residuals
961 were measures of the relative local offsets between the layer and the two reference layers,
962 quadruplets with the largest relative misalignments had the largest range of residuals. the
963 correlation plots were an easy visual way to identify quadruplets with large relative misalign-
964 ments.

965 The most significant limit on measuring the degree of correlation between the x-ray and
966 mean cosmics residuals was the uncertainty on the x-ray residuals, which stemmed from
967 the systematic uncertainty of 120 μm in the x-ray beam profile centers used to build the
968 abstract tracks. For example, in figure 6.3 the uncertainty in the x-ray residuals makes
969 detecting correlation impossible. The x-ray method was limited primarily by the systematic
970 uncertainties in the relative alignment of the platforms and the gun, especially the gun angle.

971 The analysis of certain quadruplets was limited by the availability of data. Sometimes,
972 less than three layers were surveyed for a given x-ray gun position so no residuals could
973 be calculated. Too few x-ray residuals prevented the analysis from detecting a significant
974 correlation, should it even be measurable. Often, the analysis of smaller quadruplets (placed
975 innermost on the wheel) suffered as a result because they had fewer alignment platforms, and
976 hence gun positions, on their surfaces. The analysis was also limited to certain quadruplets.
977 The wedges constructed the earliest (typically small wedges) were surveyed when the x-ray
978 method was still being designed and so have limited x-ray residuals calculated from beam
979 profiles of lower quality. In addition, not all cosmic muon test sites had enough front end
980 electronics to collect data on three layers simultaneously, which is the minimum required to
981 be able to calculate residuals.

982 Nonetheless, the comparison of x-ray and cosmics residuals was really to confirm the x-ray
983 method's ability to measure local offsets with an independent dataset. The x-ray local offsets
984 allow the calculation of relative local offsets that have been correlated to the cosmics relative
985 local offsets. Therefore, the analysis of quadruplets with relative local offsets large enough
986 to detect a correlation validates the x-ray method's ability to measure local offsets.

987 The potential of using relative local offsets calculated from cosmics data to study relative
988 alignment between sTGC layers stands on its own. For example, although the x-ray relative

989 local offsets of QL2.P.8 in figure 6.1b do not reveal a pattern, the variation in the cosmics
990 relative local offsets do. Identifying the pattern is possible because mean cosmics residuals
991 can be calculated across the entire area and are sensitive to smaller relative local offsets since
992 their uncertainty is significantly smaller.

993 The advantage of the x-ray dataset over the cosmics dataset is that absolute local offsets
994 are measurable thanks to the reference frame provided by the alignment platforms. This is
995 required to measure the position of strips in the ATLAS coordinate system to satisfy the
996 NSWs' precision tracking goals. The x-ray local offsets are being used to build an alignment
997 model of strips in each quadruplet. It is compelling to imagine using the cosmics relative
998 local offsets to improve the model considering their precision and ability to capture effects
999 across the entire area of the quadruplet.

1000 **Chapter 7**

1001 **Outlook and summary**

1002 The cosmic muon dataset was used to independently confirm the absolute local offsets mea-
1003 sured by the x-ray method. The x-ray offsets are being used to complete the sTGC alignment
1004 scheme of the NSWs: the NSW alignment system monitors the position of alignment plat-
1005 forms on the surface of sTGC wedges, and the x-ray measurements provide the offsets of
1006 the strip pattern with respect to each alignment platform. The continuation of this anal-
1007 ysis is detailed next (section 7.1) before summarizing and considering the larger context
1008 (section 7.2).

1009 **7.1 Outlook**

1010 Next all quadruplets with suitable cosmics and x-ray data should be surveyed to flag anom-
1011alous quadruplets (as a first step). If a quadruplet’s correlation plot like figure 6.2 or 6.3
1012 reveals an unexpected correlation or has a large scatter, it would indicate an issue with ei-
1013ther the cosmics or x-ray data collection to be investigated further. The uncertainty in each
1014 set of tracking points would inform the interpretation of the anomaly. Then, the quality of
1015 the correlation should be evaluated over all quadruplets instead of individually.
1016 For now, the correlation for the individual quadruplets tested support the use of the x-ray
1017 data to build an alignment model [8]. Work on creating an alignment model is ongoing.
1018 Currently, the algorithm compares the y -position of a local group of strips at each x-ray gun
1019 position as measured by the x-ray and CMM methods in a fit to extract a global slope (m)

1020 and offset (b) per layer, i , where the χ^2 is given by equation 7.1.

$$\chi^2 = \frac{[dy_{cmm,corr} - dy_{xray}]^2}{\delta dy_{xray}^2 + \delta dy_{cmm,corr}^2}, \quad (7.1)$$

1021

$$dy_{cmm,corr} = y_{cmm} + b_i + m_i x - y_{nom} \quad (7.2)$$

1022 Here, dy refers to the corrected CMM and x-ray local offsets, and δdy refers to their re-
1023 spective uncertainties. The CMM measurements were taken before the cathode boards were
1024 assembled into quadruplets, so alignment parameters for the given layer were extracted from
1025 the χ^2 fit by stepping the corrected CMM y -position towards the x-ray y -position by adjust-
1026 ing the layer's slope and offset parameters. The plan is that the alignment parameters will
1027 be provided to the ATLAS experiment's offline software to reconstruct muon tracks from the
1028 NSWs' sTGCs. The large uncertainty on the x-ray local offsets (120 μm) and the sparseness
1029 of the measurements means that including input from other characterization datasets could
1030 reduce the uncertainty on the alignment model parameters.

1031 The uncertainty in the mean cosmics residuals was smaller than the desired position reso-
1032 lution of the sTGCs, so they provide relevant information about strip positions. Moreover,
1033 they can be calculated over the entire area of the quadruplet instead of at specific posi-
1034 tions. It would be great to use the cosmics residuals as input to calculate and reduce the
1035 uncertainty on the alignment parameters. Since mean cosmics residuals can only provide
1036 relative alignment information, one idea would be to use them to constrain the fit of the
1037 alignment parameters. In this case, the alignment parameters would need to be fitted on all
1038 layers at once, and the shifting y -positions on each layer forced to create an abstracted track
1039 residual equal to the local mean cosmics residual (within uncertainty) for each x-ray point.
1040 Or, instead of constraining the fit, it could be penalized if the resulting parameters do not
1041 result in abstracted track residuals equal to the mean cosmics residuals within uncertainty.
1042 Some work on using the three datasets at once in a fit has been started.

1043 7.2 Summary

1044 The LHC [1] will be at the energy frontier of particle physics for at least the next decade,
1045 making it a unique tool with which to study particle physics. With the HL-LHC [2], high
1046 statistics on rare particle physics processes will enable more precise measurements of param-
1047 eters of the Standard Model and increase the sensitivity to signatures of physics beyond the
1048 Standard Model [3]. To capitalize on the increased collision rate, the NSWs of the ATLAS
1049 experiment must be replaced to keep the triggering and tracking performance [5].

1050 Small-strip thin gap chambers are gas ionization chambers optimized for a high rate envi-
1051 ronment [5]. Using the pad electrodes to define a region of interest makes it possible to get
1052 track segments of ~ 1 mrad angular resolution quickly, which will be used as input to check
1053 if a collision originated from the interaction point and should be triggered on or not [5, 53].
1054 sTGCs are also able to provide better than $100 \mu\text{m}$ position resolution on each detector plane
1055 to fulfill precision offline tracking requirements [6].

1056 Ultimately, the positions of the sTGC strip electrodes need to be known in ATLAS to within
1057 $\sim 100 \mu\text{m}$ so that they can deliver the required position resolution. The ATLAS alignment
1058 system will position alignment platforms on the surface of the sTGC wedge, and an alignment
1059 model will be used to position the strips with respect to the alignment platforms [5]. Input
1060 to the alignment model comes from the datasets used to characterize the quadruplets. The
1061 x-ray method [8] is used to measure offsets of strips from their nominal position to achieve
1062 this goal. The alignment model could be built on x-ray data alone, but the sparseness of
1063 and large uncertainty on the local offsets mean that the alignment model could benefit from
1064 more input. Comparing the x-ray offsets to the CMM data [7] allows the effect of inter-layer
1065 misalignments to be isolated and increases the input to the alignment model.

1066 The cosmics dataset was used to confirm the local offsets measured with the x-ray gun. It
1067 provides relative local offsets between sTGC strip layers. The 2D visualizations of relative
1068 local offsets allow personnel to quickly identify areas of misaligned strips and make hypothe-
1069 ses of the physical origin of those misalignments. The correlation seen between the x-ray and
1070 cosmics relative local offsets in quadruplets with large relative misalignments both confirms
1071 the validity of the x-ray local offsets and again is a quick way to identify quadruplets with
1072 large misalignments. Moreover, the mean of track residuals in an area is a robust estimation
1073 of the relative local offset, as shown by the estimation of systematic uncertainties; the relative
1074 local offsets for all two-fixed layer reference frames do not change by more than $100 \mu\text{m}$ given
1075 variation in data collection conditions and analysis algorithms. The cosmics relative local
1076 offsets are therefore relevant input for alignment studies and could improve the alignment
1077 model that will position each strip.

1078 Achieving the required position resolution on each layer of the NSWs in the particle track
1079 bending plane achieves the design momentum resolution for muons ejected towards the end-
1080 caps of ATLAS. Muons are important signatures of electroweak and Higgs sector events
1081 of interest for the ATLAS Collaboration’s future physics goals [5]. Being the second of two
1082 tracking technologies on the NSWs, an effective alignment model of sTGC quadruplets layers
1083 is a necessary part of making the NSWs redundant for 10 or more years of recording collisions
1084 in the High Luminosity era of the LHC.

1085 References

- 1086 [1] L Evans and P Bryant. LHC Machine. *Journal of Instrumentation*, 3(S08001), 2008.
- 1087 [2] G Apollinari, I Bejar Alonso, O Bruning, P Fessia, M Lamont, L Rossi, and L Tavian.
1088 High-Luminosity Large Hadron Collider (HL-LHC) Technical Design Report V. 0.1.
1089 Technical report, CERN, Geneva, September 2017.
- 1090 [3] A Dainese et al. The physics potential of HL-LHC. In *Input to the European Particle
1091 Physics Strategy Update*, November 2018.
- 1092 [4] The ATLAS Collaboration. The ATLAS Experiment at the CERN Large Hadron Col-
1093 linder. *Journal of Instrumentation*, 3(08):S08003, 2008.
- 1094 [5] T Kawamoto, S Vlachos, L Pontecorvo, J Dubbert, G Mikenberg, P Iengo, C Dallapic-
1095 colà, C Amelung, L Levinson, R Richter, and D Lellouch. New Small Wheel Technical
1096 Design Report. Technical report, Jun 2013. ATLAS New Small Wheel Technical Design
1097 Report.
- 1098 [6] Angel Abusleme et al. Performance of a Full-Size Small-Strip Thin Gap Chamber Pro-
1099 totype for the ATLAS New Small Wheel Muon Upgrade. *Nuclear Instruments and
1100 Methods in Physics Research Section A: Accelerators, Spectrometers, Detectors and As-
1101 sociated Equipment*, 817:85–92, May 2016. arXiv: 1509.06329.
- 1102 [7] Evan Michael Carlson. *Results of the 2018 ATLAS sTGC test beam and internal strip
1103 alignment of sTGC detectors*. Thesis, University of Victoria, Victoria, Canada, 2019.
1104 Accepted: 2019-07-16T17:20:40Z.
- 1105 [8] B. Lefebvre. Precision survey of the readout strips of small-strip Thin Gap Chambers
1106 using X-rays for the muon spectrometer upgrade of the ATLAS experiment. *Journal of
1107 Instrumentation*, 15(07):C07013–C07013, July 2020.

- 1108 [9] David J. Griffiths. *Introduction to elementary particles*. Physics textbook. Wiley-VCH,
 1109 Weinheim, Germany, 2., rev. ed., 5. reprint edition, 2011.
- 1110 [10] Michael Edward Peskin and Daniel V. Schroeder. *An introduction to quantum field
 1111 theory*. Addison-Wesley Pub. Co, Reading, Massachusetts, 1995.
- 1112 [11] P.A. Zyla et al. Review of Particle Physics. *PTEP*, 2020(8):083C01, 2020.
- 1113 [12] Makoto Kobayashi and Toshihide Maskawa. CP-violation in the renormalizable theory
 1114 of weak interaction. *Progress of theoretical physics*, 49(2):652–657, February 1973.
- 1115 [13] M. L. Perl, G. S. Abrams, A. M. Boyarski, M. Breidenbach, D. D. Briggs, F. Bulos,
 1116 W. Chinowsky, J. T. Dakin, G. J. Feldman, C. E. Friedberg, D. Fryberger, G. Goldhaber,
 1117 G. Hanson, F. B. Heile, B. Jean-Marie, J. A. Kadyk, R. R. Larsen, A. M. Litke, D. Lüke,
 1118 B. A. Lulu, V. Lüth, D. Lyon, C. C. Morehouse, J. M. Paterson, F. M. Pierre, T. P.
 1119 Pun, P. A. Rapidis, B. Richter, B. Sadoulet, R. F. Schwitters, W. Tanenbaum, G. H.
 1120 Trilling, F. Vannucci, J. S. Whitaker, F. C. Winkelmann, and J. E. Wiss. Evidence
 1121 for Anomalous Lepton Production in $\{e\}^+ \rightarrow \{e\}^- \{e\}^+ \rightarrow \{e\}^-$ Annihilation. *Physical Review Letters*, 35(22):1489–1492, December 1975. Publisher:
 1122 American Physical Society.
- 1123 [14] F. Englert and R. Brout. Broken Symmetry and the Mass of Gauge Vector Mesons.
Physical Review Letters, 13(9):321–323, August 1964. Publisher: American Physical
 1124 Society.
- 1125 [15] P. W. Higgs. Broken symmetries, massless particles and gauge fields. *Physics Letters*,
 1126 12(2):132–133, September 1964.
- 1127 [16] David Galbraith and Carsten Burgard. UX: Standard Model of the Standard Model,
 1128 November 2013.
- 1129 [17] Carlos A. Bertulani. *Nuclear physics in a nutshell*. In a nutshell. Princeton University
 1130 Press, Princeton, N.J, 2007. OCLC: ocm85690422.
- 1131 [18] Bradley W. Carroll and Dale A. Ostlie. *An introduction to modern astrophysics*. Pearson
 1132 Addison-Wesley, San Francisco, 2nd ed edition, 2007. OCLC: ocm69020924.
- 1133 [19] Mirko Boezio and Emiliano Mocchiutti. Chemical composition of galactic cosmic rays
 1134 with space experiments. *Astroparticle Physics*, 39-40:95–108, December 2012.
- 1135 [20] B. Aharmim et al. Combined analysis of all three phases of solar neutrino data from
 1136 the sudbury neutrino observatory. *Phys. Rev. C*, 88:025501, Aug 2013.

- 1139 [21] B. Pontecorvo. Neutrino Experiments and the Problem of Conservation of Leptonic
 1140 Charge. *Zh. Eksp. Teor. Fiz.*, 53:1717–1725, 1967.
- 1141 [22] S. M. Bilenky and S. T. Petcov. Massive neutrinos and neutrino oscillations. *Reviews*
 1142 *of Modern Physics*, 59(3):671–754, July 1987.
- 1143 [23] Bing-Lin Young. A survey of dark matter and related topics in cosmology. *Frontiers of*
 1144 *Physics*, 12(2):121201, April 2017.
- 1145 [24] Carlos Muñoz. Dark matter detection in the light of recent experimental results. *International*
 1146 *Journal of Modern Physics A*, 19(19):3093–3169, July 2004.
- 1147 [25] Gerard Jungman, Marc Kamionkowski, and Kim Griest. Supersymmetric dark matter.
 1148 *Physics Reports*, 267(5):195–373, March 1996.
- 1149 [26] G. Arnison et al. Experimental observation of isolated large transverse energy elec-
 1150 trons with associated missing energy at $s=540$ GeV. *Physics Letters B*, 122(1):103–116,
 1151 February 1983.
- 1152 [27] M. Banner et al. Observation of single isolated electrons of high transverse momentum
 1153 in events with missing transverse energy at the CERN pp collider. *Physics Letters B*,
 1154 122(5):476–485, March 1983.
- 1155 [28] G. Arnison et al. Experimental observation of lepton pairs of invariant mass around 95
 1156 GeV/c² at the CERN SPS collider. *Physics Letters B*, 126(5):398–410, July 1983.
- 1157 [29] P. Bagnaia et al. Evidence for $Z \rightarrow e^+e^-$ at the CERN pp collider. *Physics Letters B*,
 1158 129(1):130–140, 1983.
- 1159 [30] CDF Collaboration. Observation of Top Quark Production in
 1160 $\overline{p}p$ Collisions with the Collider Detector at Fermilab. *Physical Review Letters*, 74(14):2626–2631, April 1995. Publisher: American
 1161 Physical Society.
- 1163 [31] D0 Collaboration. Observation of the Top Quark. *Physical Review Letters*, 74(14):2632–
 1164 2637, April 1995. Publisher: American Physical Society.
- 1165 [32] The ATLAS Collaboration. Observation of a new particle in the search for the Standard
 1166 Model Higgs boson with the ATLAS detector at the LHC. *Physics Letters B*, 716(1):1–
 1167 29, September 2012. arXiv: 1207.7214.

- 1168 [33] The CMS Collaboration. Observation of a new boson at a mass of 125 GeV with the
1169 CMS experiment at the LHC. *Physics Letters B*, 716(1):30–61, September 2012. arXiv:
1170 1207.7235.
- 1171 [34] Standard Model Summary Plots June 2021.
- 1172 [35] The ALICE Collaboration. The ALICE experiment at the CERN LHC. *JOURNAL OF*
1173 *INSTRUMENTATION*, 3, AUG 2008.
- 1174 [36] ATLAS luminosity public results run-1, March 2011.
- 1175 [37] ATLAS luminosity public results run-2, July 2015.
- 1176 [38] The European Strategy for Particle Physics. Technical Report CERN/2685, CERN,
1177 2006. Adopted by the CERN council at a special session at ministerial level in Lisbon
1178 in 2006.
- 1179 [39] HiLumi HL-LHC Project. LHC/HL-LHC plan (last update january 2021). <https://hilumilhc.web.cern.ch/content/hl-lhc-project>, last accessed on 2021-09-09.
- 1180
- 1181 [40] M. Cepeda et al. Report from Working Group 2: Higgs Physics at the HL-LHC and
1182 HE-LHC. *CERN Yellow Rep. Monogr.*, 7:221–584. 364 p, Dec 2018.
- 1183 [41] ATLAS inner detector : Technical Design Report, 1. Technical Report CERN-LHCC-
1184 97-016, CERN, 1997. ISBN: 9789290831020 Publication Title: CERN Document Server.
- 1185 [42] L. Rossi, S. Haywood, A. Romanouk, and R. Nickerson. ATLAS inner detector : Tech-
1186 nical Design Report, 2. Technical Report CERN-LHCC-97-017, CERN, 1997. ISBN:
1187 9789290831037 Publication Title: CERN Document Server.
- 1188 [43] ATLAS liquid-argon calorimeter : Technical Design Report. Technical Report CERN-
1189 LHCC-96-041, CERN, 1996. ISBN: 9789290830900 Publication Title: CERN Document
1190 Server.
- 1191 [44] ATLAS tile calorimeter : Technical Design Report. Technical Report CERN-LHCC-96-
1192 042, CERN, 1996. ISBN: 9789290830917 Publication Title: CERN Document Server.
- 1193 [45] ATLAS level-1 trigger : Technical Design Report. Technical Report CERN-LHCC-98-
1194 014, CERN, 1998. ISBN: 9789290831280 Publication Title: CERN Document Server.
- 1195 [46] Technical Design Report for the Phase-II Upgrade of the ATLAS TDAQ System. Tech-
1196 nical report, CERN, Geneva, Sep 2017.

- 1197 [47] Marzio Nessi, Markus Nordberg, Peter Jenni, and Kenway Smith. ATLAS high-level
1198 trigger, data-acquisition and controls : Technical Design Report. Technical Report
1199 CERN-LHCC-2003-022, CERN, 2003. Publication Title: CERN Document Server.
- 1200 [48] A Ruiz Martínez and. The run-2 ATLAS trigger system. *Journal of Physics: Conference*
1201 *Series*, 762:012003, oct 2016.
- 1202 [49] ATLAS magnet system : Technical Design Report, 1. Technical Report CERN-LHCC-
1203 97-018, CERN, 1997. ISBN: 9789290831044 Publication Title: CERN Document Server.
- 1204 [50] ATLAS Collaboration. Performance of the ATLAS muon trigger in pp collisions at
1205 $\sqrt{s}=8\text{ TeV}$. *The European Physical Journal C*, 75(3):120, March 2015. arXiv:
1206 1408.3179.
- 1207 [51] ATLAS Collaboration. ATLAS Muon Spectrometer: Technical Design Report. Techni-
1208 cal Report CERN-LHCC-97-022, CERN, Geneva, 1997.
- 1209 [52] S. Aefsky, C. Amelung, J. Bensinger, C. Blocker, A. Dushkin, M. Gardner, K. Hashemi,
1210 E. Henry, B. Kaplan, P. Keselman, M. Ketchum, U. Landgraf, A. Ostapchuk, J. Roth-
1211 berg, A. Schricker, N. Skvorodnev, and H. Wellenstein. The Optical Alignment System
1212 of the ATLAS Muon Spectrometer Endcaps. *Journal of Instrumentation*, 3(11):P11005–
1213 P11005, November 2008. Publisher: IOP Publishing.
- 1214 [53] E. Perez Codina. Small-strip Thin Gap Chambers for the muon spectrometer upgrade of
1215 the ATLAS experiment. *Nuclear Instruments and Methods in Physics Research Section*
1216 *A: Accelerators, Spectrometers, Detectors and Associated Equipment*, 824:559–561, July
1217 2016.
- 1218 [54] John Townsend. *Electricity in gases*. Clarendon Press, Oxford, 1915.
- 1219 [55] S. Majewski, G. Charpak, A. Breskin, and G. Mikenberg. A thin multiwire chamber
1220 operating in the high multiplication mode. *Nuclear Instruments and Methods*, 217:265–
1221 271, 1983.
- 1222 [56] E. Gatti, A. Longoni, H. Okuno, and P. Semenza. Optimum geometry for strip cathodes
1223 or grids in MWPC for avalanche localization along the anode wires. *Nuclear Instruments*
1224 *and Methods*, 163(1):83–92, July 1979.
- 1225 [57] G. Battistoni, P. Campana, V. Chiarella, U. Denni, E. Iarocci, and G. Nicoletti. Re-
1226 sistive cathode transparency. *Nuclear Instruments and Methods in Physics Research*,
1227 202(3):459–464, November 1982.

- 1228 [58] P. K. F. Grieder. *Cosmic rays at Earth: researcher's reference manual and data book*.
 1229 Elsevier Science Ltd, Amsterdam, 1st ed edition, 2001.
- 1230 [59] Benoit Lefebvre. *Characterization studies of small-strip Thin Gap Chambers for the*
 1231 *ATLAS Upgrade*. PhD Dissertation, McGill University, Montreal, Canada, 2018.
- 1232 [60] R. Keyes, K.A. Johnson, L. Pepin, F. Léger, C. Qin, S. Webster, A. Robichaud-
 1233 Véronneau, C. Bélanger-Champagne, B. Lefebvre, S.H. Robertson, A. Warburton,
 1234 B. Vachon, and F. Corriveau. Development and characterization of a gas system and
 1235 its associated slow-control system for an ATLAS small-strip thin gap chamber testing
 1236 facility. *Journal of Instrumentation*, 12(04):P04027–P04027, April 2017.
- 1237 [61] George Iakovidis. VMM3, an ASIC for Micropattern Detectors. In *Proceedings of*
 1238 *Science*, page 5, Philadelphia, 2017.
- 1239 [62] Bohan Chen. *Calibration Studies of the Front-End Electronics for the ATLAS New*
 1240 *Small Wheel Project*. PhD thesis, McGill University, Montreal, Canada, 2019.
- 1241 [63] R. Brun and F. Rademakers. ROOT: An object oriented data analysis framework.
 1242 *Nucl. Instrum. Meth. A*, 389:81–86, 1997. See also "ROOT" [software], Release 6.18/02,
 1243 23/08/2019, (<https://zenodo.org/record/3895860#.YVJW6n0pCHs>).
- 1244 [64] Fabio Sauli. Principles of operation of multiwire proportional and drift chambers. In *Cern*
 1245 *Yellow Reports: Monographs*, page 92 p, Geneva, 1977. CERN, CERN. CERN,
 1246 Geneva, 1975 - 1976.
- 1247 [65] M. Hatlo, F. James, P. Mato, L. Moneta, M. Winkler, and A. Zsenei. Developments
 1248 of mathematical software libraries for the LHC experiments. *IEEE Trans. Nucl. Sci.*,
 1249 52:2818–2822, 2005.
- 1250 [66] Hongwei Guo. A Simple Algorithm for Fitting a Gaussian Function [DSP Tips and
 1251 Tricks]. *IEEE Signal Processing Magazine*, 28(5):134–137, September 2011.
- 1252 [67] Ichita Endo, Tatsuo Kawamoto, Yoshinari Mizuno, Takashi Ohsugi, Takashi Taniguchi,
 1253 and Tohru Takeshita. Systematic shifts of evaluated charge centroid for the cathode
 1254 read-out multiwire proportional chamber. *Nuclear Instruments and Methods in Physics*
 1255 *Research*, 188(1):51–58, September 1981.
- 1256 [68] Bernd Stelzer. The New Small Wheel Upgrade Project of the ATLAS Experiment.
 1257 *Nuclear and Particle Physics Proceedings*, 273-275:1160–1165, April 2016.

- 1258 [69] Xiao Zhao, Wenlong Li, Dengfeng Zhang, Changyu Li, Han Li, Shengquan Liu, Peng
1259 Miao, Yanyan Du, Yanyun Duan, and Chengguang Zhu. Cosmic test of sTGC detector
1260 prototype made in China for ATLAS experiment upgrade. *Nuclear Instruments and Methods in Physics Research Section A: Accelerators, Spectrometers, Detectors and Associated Equipment*, 927:257–261, May 2019.
- 1263 [70] Manfred Krammer. Upgrade Programs of the LHC Experiment, November 2017.
- 1264 [71] Benoit Lefebvre. stgc_as_built_fit.
- 1265 [72] Benoit Lefebvre. tgc_analysis.
- 1266 [73] The ATLAS Collaboration. Athena.
- 1267 [74] Lia Formenti. cosmics_xray_correlation.
- 1268 [75] Siyuan Sun. sTGC_readout_sw.
- 1269 [76] G Brianti. Large Hadron Collider in the LEP Tunnel. In *Proceedings of the ECFA-CERN Workshop*, volume 1, page 352, Lausanne and Geneva, March 1984.
- 1271 [77] Letter of Intent for the Phase-I Upgrade of the ATLAS Experiment. Technical Report
1272 CERN-LHCC-2011-012. LHCC-I-020, CERN, Geneva, November 2011.
- 1273 [78] ATLAS: letter of intent for a general-purpose pp experiment at the large hadron collider
1274 at CERN. Technical Report CERN-LHCC-92-004, CERN, Geneva, 1992.
- 1275 [79] The ATLAS Collaboration. Technical Design Report for the Phase-I Upgrade of the
1276 ATLAS TDAQ System. Technical report, Sep 2013. Final version presented to December
1277 2013 LHCC.
- 1278 [80] Howard Georgi and S. L. Glashow. Unity of all elementary-particle forces. *Phys. Rev. Lett.*, 32:438–441, Feb 1974.
- 1280 [81] Luca Lista. *Statistical Methods for Data Analysis in Particle Physics*, volume 941 of
1281 *Lecture Notes in Physics*. Springer International Publishing, Cham, 2017.
- 1282 [82] K. Kodama et al. Detection and analysis of tau neutrino interactions in DONUT
1283 emulsion target. *Nucl. Instrum. Meth. A*, 493:45–66, 2002.

¹²⁸⁴ APPENDICES

1285 **Appendix A**

1286 **Uncertainty in cluster positions**

1287 **A.1 Cluster definition**

1288 A cluster is a series of contiguous strip channels on a layer with non-zero amplitude, all
1289 part of the same trigger and having the same event number [59]. Clusters result from the
1290 drift of ionization products generate in the ionization avalanche caused by a muon [54]. The
1291 peak-detector-output (PDO) of the signal on each strip of a cluster is fit with a Gaussian.
1292 The y-position of a particle as it passed through the layer is mean of the cluster, referred to
1293 here as the hit position.

1294 **A.2 Effect of fit algorithm on cluster mean**

1295 The clusters were fit with Guo's method [66] and Minuit2 for ROOT [65]. The difference in
1296 cluster means between the two algorithms is shown in figure A.1.

1297 The RMS of the distribution in figure A.1 is 57 μm , which is much larger than the statistical
1298 uncertainty in the mean for the Minuit2 algorithm, which peaks around 7 μm . An RMS of
1299 60 μm is common for data taken with most quadruplets at 3.1 kV. Therefore, the uncertainty
1300 in the y-hit positions is assigned 60 μm .

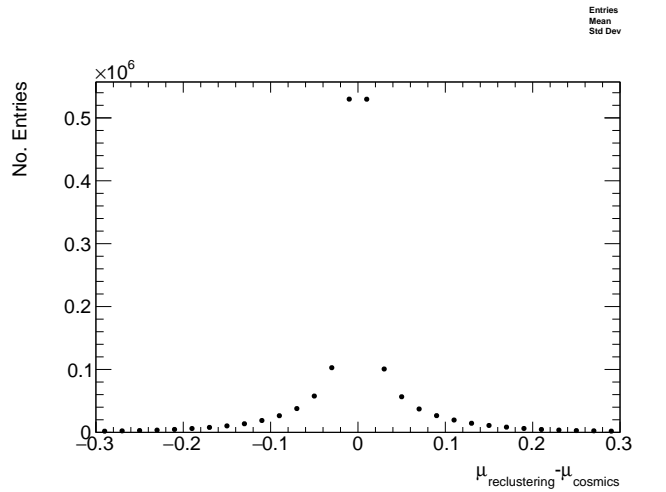


Figure A.1: The difference between cluster means calculated with Guo's method [66] in `tgc_analysis/CosmicsAnalysis` and `Minuit2` for `ROOT` [65] in `strip_position_analysis/ReClustering` for data collected with QL2.P.8 at 3.1 kV.

1301 **A.3 Effect of uncertainty in cluster mean on track residuals**

1302

1303 The uncertainty assigned to the hit position affected the uncertainty in the extrapolated/interpolated
1304 position of the track, and in the residuals. The bin size of the residual distributions was set
1305 to 200 μm because that was the uncertainty in the residuals calculated from the tracks with
1306 the least favourable geometry (like tracks built from hits on layers 1 and 2 and extrapolated
1307 to layer 4).

1308 **Appendix B**

1309 **Study of cosmics for alignment
1310 analysis statistical uncertainty**

1311 Typically, one million triggers (cosmic muon events, noise, photons and δ -rays) were collected
1312 for each Canadian quadruplet at McGill University, resulting in roughly half the number of
1313 viable tracks after cuts. For QS3.P.18, 3.5 million triggers were collected. To gauge the
1314 sensitivity of the analysis to the available statistics, partitions of this data with each with
1315 a different number of triggers were analyzed separately. Ultimately, the quantity of interest
1316 was the gaussian mean of the residual distribution in regions of interest, so the peak in the
1317 distribution of the statistical uncertainty in the residual means for each area of interest for
1318 a specific tracking combination was used to gauge the quality of the analysis. How the peak
1319 in the residual mean uncertainty distribution changes with the number of triggers is shown
1320 in figure for tracks on layer 1 built from layers 3 and 4 [B.1](#).

1321 The uncertainty is already around 20 μm at 1 million triggers, suitable for distinguishing
1322 differences in offsets of order 50 μm as required. Although increased statistics could decrease
1323 the statistical uncertainty, it is not required for the goals of this analysis. Moreoever, the
1324 systematic uncertainty is around 50 μm and the systematic uncertainty on the x-ray residuals
1325 is 150 μm so the statistical uncertainty of 20 μm is nearly negligible.

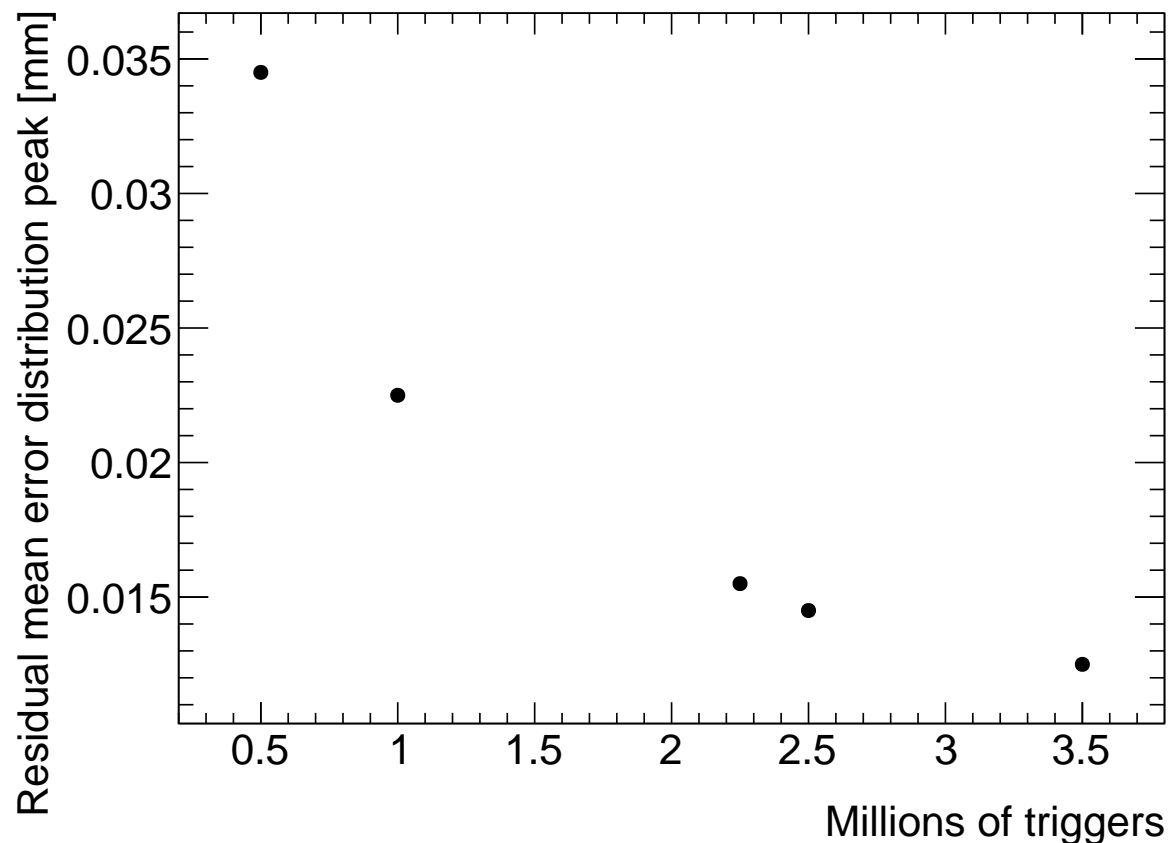


Figure B.1: How the peak of the distributions of uncertainties in the residual means in regions of interest for tracks on layer 1 built from layers 3 and 4 changed with the number of triggers used in the analysis. The distribution falls off as $\frac{1}{\sqrt{N}}$ as expected.

1326 Appendix C

1327 Study of systematic uncertainties 1328 when using cosmics data for 1329 alignment studies

1330 C.1 Residual distribution fit function

1331 The distribution of residuals should be modelled by a double gaussian fit[59]:

$$G(r) = A_s \exp \left[\frac{-(r - \mu)^2}{2\sigma_s^2} \right] + A_b \exp \left[\frac{-(r - \mu)^2}{2\sigma_b^2} \right] \quad (\text{C.1})$$

1332 where r is the residual, A is the gaussian amplitude, μ is the gaussian mean, σ is the
1333 gaussian sigma, and the subscripts s and b stand for signal and background respectively.
1334 One gaussian captures the real (signal) tracks and the other captures the tracks built from
1335 noise (background). The gaussian with the smaller width is identified as the signal.

1336 A single gaussian fit failed less often than a double gaussian fit. The gaussian fits were
1337 performed by initially estimating the amplitude to be 100 tracks, the gaussian mean to be
1338 the histogram mean, and gaussian σ to be the RMS. The fit range was restricted to ± 1 RMS
1339 from the histogram mean. The modification helped the gaussian fit capture the signal peak.
1340 An example residual distribution is shown in figure C.1.

1341 For all residual distributions in 100 mm by 100 mm bins on layer 4 built from hits on layers 1
1342 and 2, the difference in gaussian and double gaussian means and σ 's is shown in figure C.2.
1343 Since the RMS of the residual mean differences distribution is less than 50 μm the gaussian

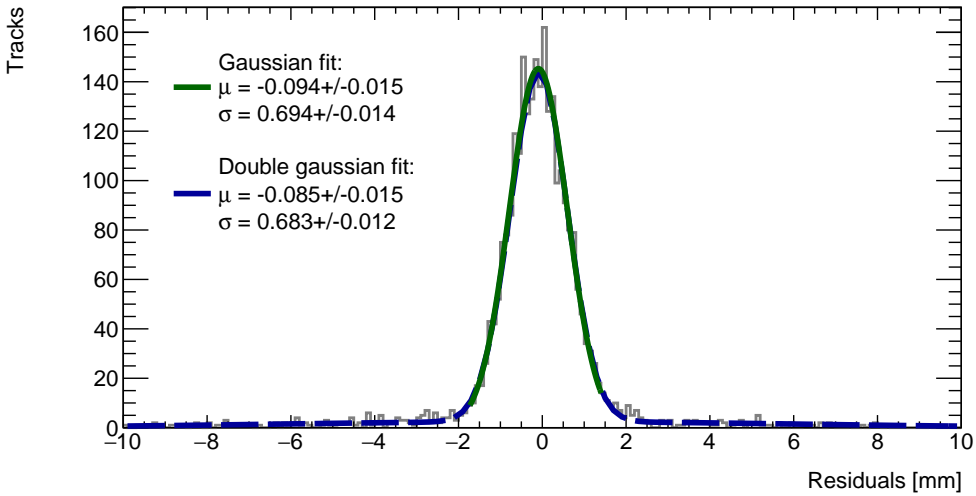


Figure C.1: Residual distribution for tracks on layer 4 built from hits on layers 1 and 2 for $x \in [-3.00, 97.00]$, $y \in [394.60, 494.60]$ mm for QL2.P.8 fit with a double gaussian and a single gaussian in a range of ± 1 RMS from the histogram mean.

1344 fit gave the same result within the required precision. Moreover, this is for the tracking
1345 combination with the worst extrapolation lever arm and the widest distribution of mean
1346 differences; the interpolation combinations have narrower distributions.

1347 The gaussian σ should be larger than the double gaussian σ because the gaussian distribution
1348 includes the effect of the noise tracks with large residuals, while the double gaussian models
1349 signal and background residuals separately. For this analysis, only the residual mean was
1350 important, so the systematic overestimate of the signal σ in the gaussian fit shown on the
1351 right of figure C.2 was allowed.

1352 C.2 Cosmic muon data collection voltage

1353 Cosmic muon data was collected at 2.9 kV and 3.1 kV because although 2.9 kV is closer to
1354 the operating conditions the chambers will be subject to in ATLAS, the extra gain provided
1355 by operating at 3.1 kV increased the signal to noise ratio for pad signals. Also, the tracking
1356 efficiency was higher with data collected at 3.1 kV. The difference in gain affected the relative
1357 population of clusters of different sizes, which in turn affected the uncertainty in the strip hit
1358 positions on each layer, the uncertainty in the track positions and the residual distributions.
1359 The residual distributions for 3.1 kV data are narrower, as shown in figure C.3.

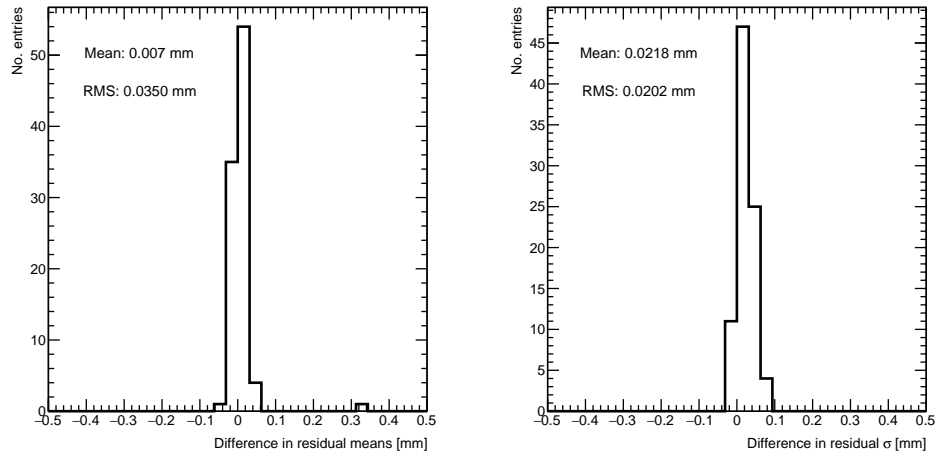


Figure C.2: Difference in residual distribution means and σ 's for a gaussian and double gaussian fit, for all residual distributions in 100 mm by 100 mm bins on layer 4 built from hits on layers 1 and 2 for QL2.P.8.

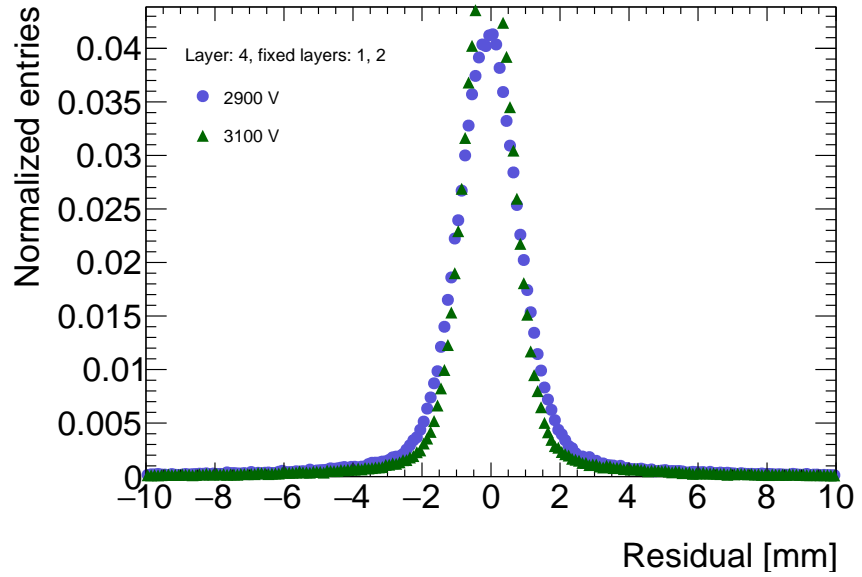


Figure C.3: Residual distribution for tracks on layer 4 built from hits on layers 1 and 2 for QL2.P.8 for data collected at 2.9 kV and 3.1 kV.

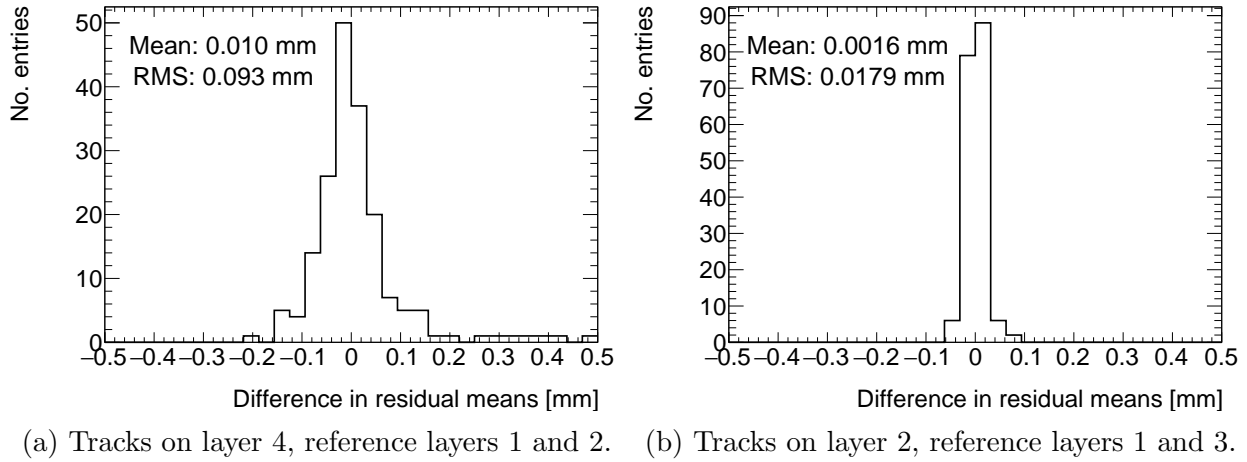


Figure C.4: Difference in residual means for data collected with QL2.P.8 at 2.9 kV and 3.1 kV respectively in 100 mm by 100 mm bins for (a) tracks on layer 4 built from hits on layers 1 and 2 and (b) tracks on layer 2 built from hits on layers 1 and 3.

1360 Neither dataset is better for calculating the mean of residuals in a given area, so a systematic
 1361 uncertainty can be assigned based on the difference in residual means calculated for 2.9 kV
 1362 and 3.1 kV data; namely, the systematic uncertainty was approximated as the RMS of the
 1363 residual mean difference distribution. Data taken with QL2.P.8 was used to estimate the
 1364 RMS, as in figure C.4a.

1365 Tracks built from hits on layers 1 and 2 and extrapolated to layer 4 have the worst lever arm
 1366 and hence the most uncertainty. The width of the distribution for geometrically favourable
 1367 tracks are much narrower. The narrowest width of the residual mean difference distribution
 1368 is for tracks on layer 2 built from hits on layers 1 and 3 (see figure C.4b).

1369 Therefore, for each tracking combination, a systematic uncertainty equal to the RMS of the
 1370 residual mean difference distribution was assigned.

1371 C.3 Cluster fit algorithm

1372 To ensure that changing the cluster fitting algorithm like in appendix A would not change
 1373 the calculated mean of residuals in each region of interest significantly, the residual means
 1374 were compared in both cases. The distribution of the difference in residual means is plotted
 1375 in figure C.5 for the tracking combination with the worst extrapolation lever arm.

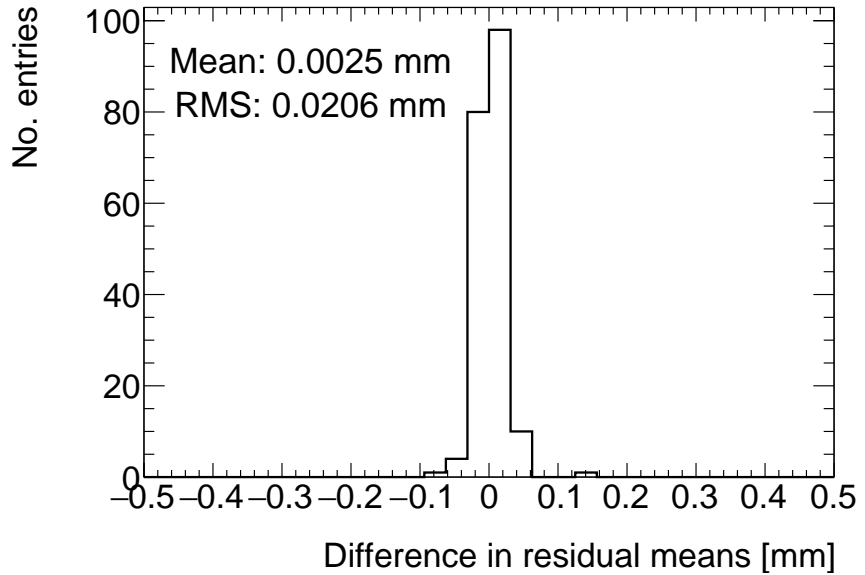


Figure C.5: Difference in residual means when the cluster fit algorithm is `Minuit2` [65] versus Guo’s method [66] for tracks on layer 4 built from hits on layers 1 and 2 for QL2.P.8.

1376 The other tracking combinations had smaller RMS values. Differences on the order of 50 μm
 1377 are important, so figure C.5 shows that the clustering algorithm had a small but notable
 1378 effect. Therefore, the RMS for each tracking combination will be used to add a systematic
 1379 uncertainty on the residual means.

1380 C.4 Differential non-linearity

1381 Definition

1382 In this context, differential non-linearity (DNL) is when the reconstructed cluster mean is
 1383 biased by the fit of the discretely sampled PDO distribution over the strips. The bias depends
 1384 on the relative position of the avalanche with respect to the center of the closest strip. For a
 1385 summary of DNL, refer to page 40 of Lefebvre’s thesis [59] and for an example application,
 1386 refer to [6].

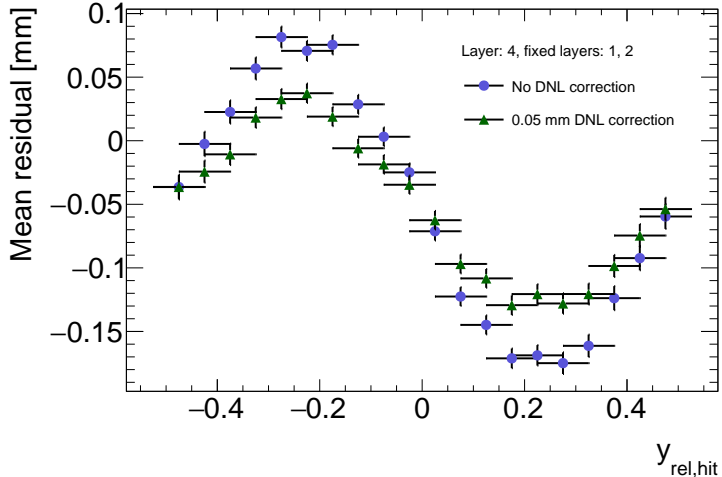


Figure C.6: Effect applying a 50 μm DNL correction to the cluster means on the residual vs y_{rel} distribution for tracks built from layers 1 and 2 and extrapolated to layer 4 for QL2.P.8.

Application and effect of DNL

The cluster mean was corrected for DNL using the equation:

$$y' = y + a \sin(2\pi y_{rel}) \quad (\text{C.2})$$

where y is the cluster mean, y_{rel} is the relative position of the cluster mean with respect to the strip's center, a is the amplitude of the correction, and y' is the corrected cluster mean. The amplitude can be derived by comparing the reconstructed hit position to the expected hit position, as done in Abusleme, 2016 [6]. With cosmic muons, there is no reference hit position to compare to, so track residuals were used as a proxy [59]. The hallmark of the DNL effect is the periodic pattern in the residual versus y_{rel} profile, and the effect of correcting the cluster means using an amplitude of 50 μm is shown in figure C.6. An amplitude of 50 μm was based on Lefebvre's estimate of the DNL amplitudes by layer, quadruplet and cluster size using exclusive cosmic muon tracks in `tgc_analysis/CosmicsAnalysis`. Little variation was seen in the amplitude parameters with respect to the quadruplet tested, the layer and the cluster size so a universal correction was used.

Although the correction is not large enough in this case, the figure shows that the correction does reduce the DNL effect. Slightly better performance is seen in the interpolation tracking combinations where the quality of the residuals is better. DNL corrections for cosmic muon data are difficult because the DNL effect is obscured by the effect of misalignments and

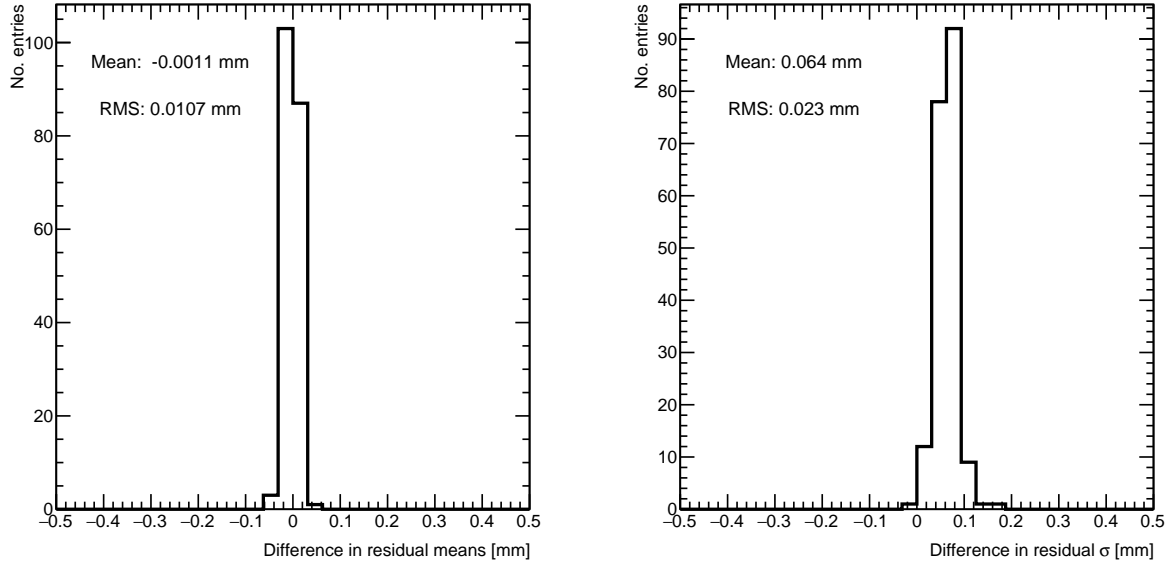


Figure C.7: Difference in residual distribution means and σ 's with and without DNL correction for residuals on layer 4 from reference layers 1 and 2 for QL2.P.8.

1404 noise. Misalignments cause the center of the sine pattern in figure C.6 to be shifted off of
 1405 zero, since the mean of residuals is shifted.

1406 In figure C.7, it is apparent that the effect of the DNL correction on the mean of the
 1407 residual distribution in 100 mm by 100 mm areas is on the order of micrometers in the worst
 1408 extrapolation case. Although the σ 's of the residual distributions shrink with the DNL
 1409 correction, the mean is the parameter of interest. Therefore, for this analysis DNL was not
 1410 corrected for.

1411 The σ 's of the residual distributions do shrink with the DNL correction but not so much to
 1412 affect the residual means, which are the important parameter for this analysis. Therefore,
 1413 since the effect of the DNL correction is negligible, it was not pursued further.

₁₄₁₄ Appendix D

₁₄₁₅ Printable plots

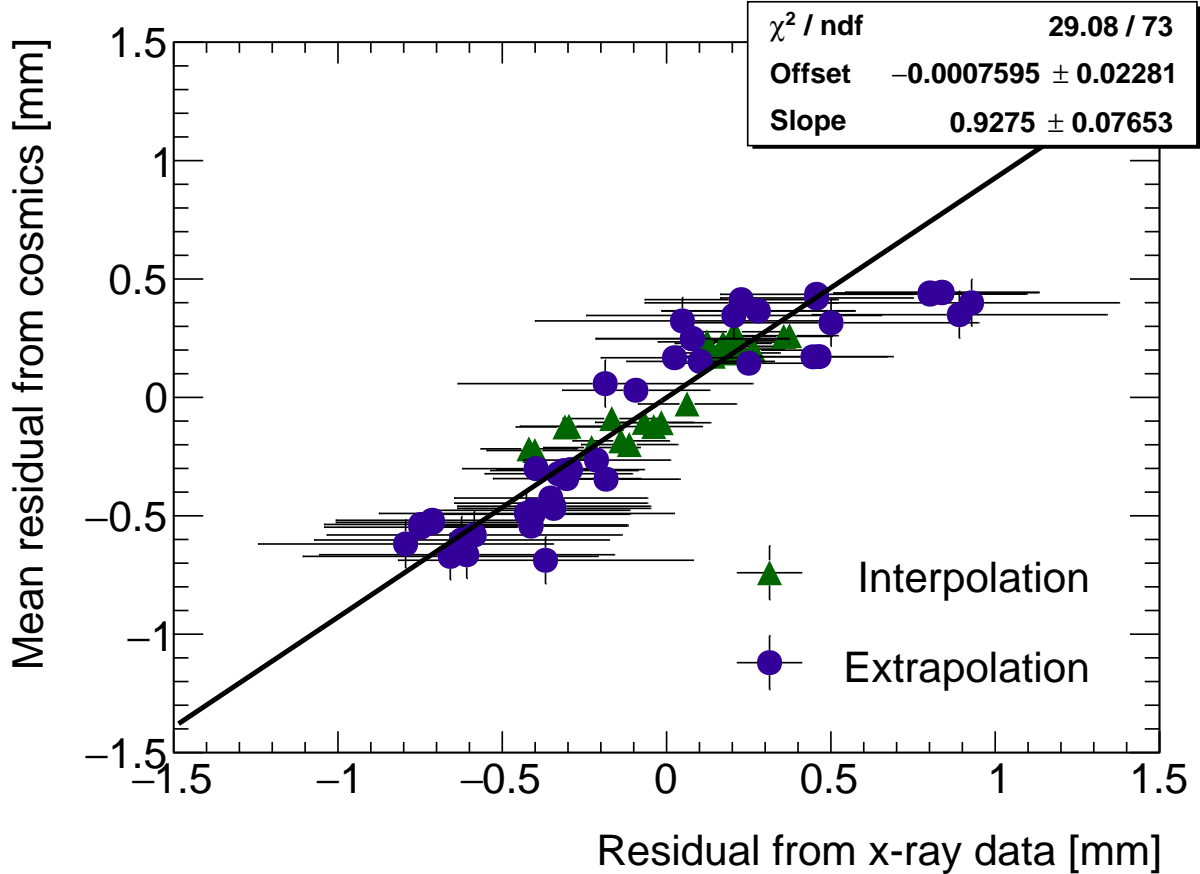


Figure D.1: Correlation plot between x-ray and cosmics residuals for all tracking combinations for QL2.P.11. Each rectangle is centered on an x-ray and mean cosmics residual pair. The width of the rectangles in x and y are the uncertainty in the x-ray and mean cosmics residual respectively. This is a printable version of figure 6.2 in section 6.1.

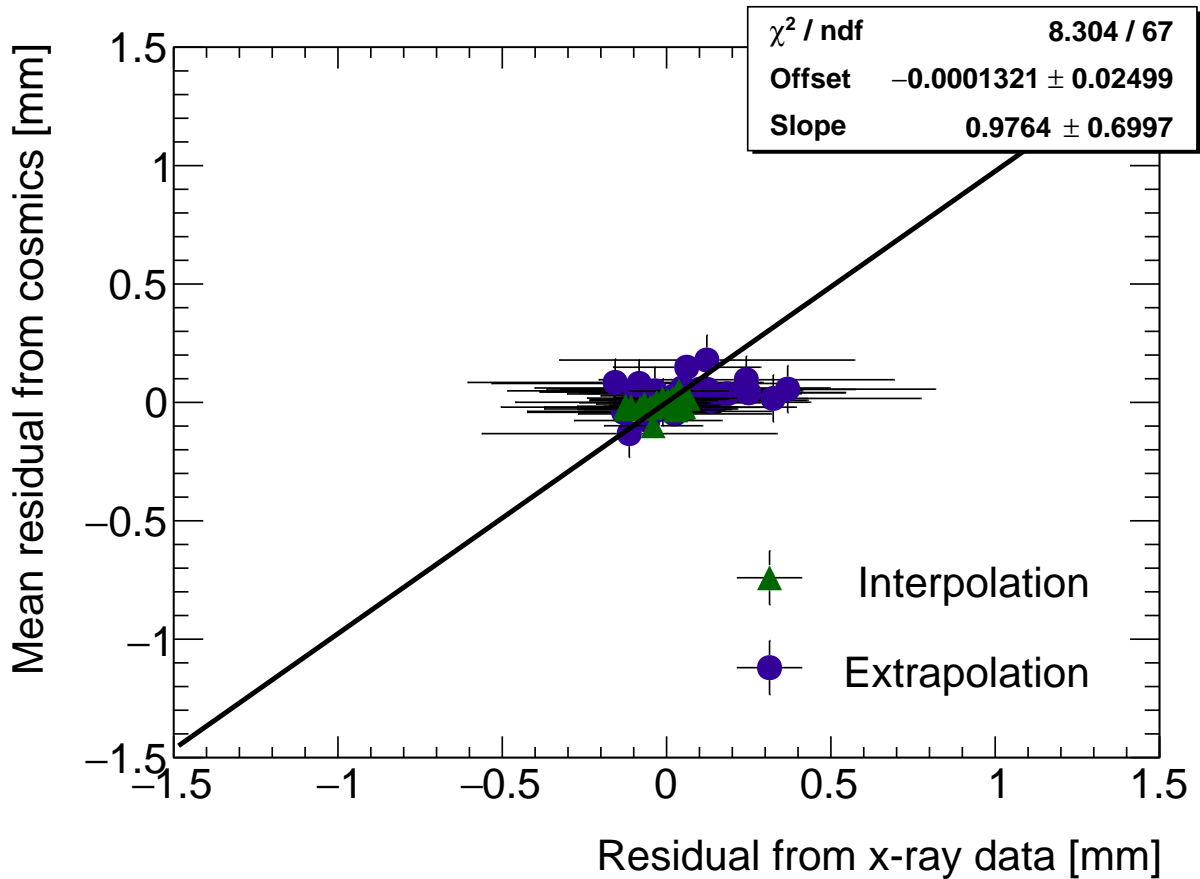


Figure D.2: Correlation plot between x-ray and cosmics residuals for all tracking combinations for QL2.P.8. Each rectangle is centered on an x-ray and mean cosmics residual pair. The width of the rectangles in x and y are the uncertainty in the x-ray and mean cosmics residual respectively. This is a printable version of figure 6.3 in section 6.1.